International Journal for Numerical Methods in Engineering

WILEY

RESEARCH ARTICLE

An Extended B-Spline-Based Material Point Method for Contact Problems

Emmanouil G. Kakouris[1] | Manolis N. Chatzis[2] | Savvas Triantafyllou[3]

[1]School of Engineering, University of Warwick, Coventry, UK | [2]Department of Engineering Science, University of Oxford, Oxford, UK | [3]Laboratory for Structural Analysis and Aseismic Research, School of Civil Engineering, National Technical University of Athens, Athens, Greece

Correspondence: Emmanouil G. Kakouris (Emmanouil.Kakouris@warwick.ac.uk)

Received: 13 September 2024 | **Revised:** 16 January 2025 | **Accepted:** 20 January 2025

Funding: This work was supported by the HORIZON EUROPE Marie Sklodowska-Curie Actions (doi: 10.13039/100018694), Engineering and Physical Sciences Research Council (doi: 10.13039/501100000266) under Grant EP/S022848/1, and Marie Sklodowska – Curie Individual Fellowship under Grant 101021629.

Keywords: extended B-Splines | frictional contact mechanics | material point method

ABSTRACT

A novel Material Point Method (MPM) is introduced for addressing contact problems. In contrast to the standard multi-velocity field approach, this method employs a penalty method to evaluate contact forces at the discretised boundaries of their respective physical domains. This enhances simulation fidelity by accurately considering the deformability of the contact surface and preventing fictitious gaps between bodies in contact. Additionally, the method utilises the Extended B-Splines (EBSs) domain approximation, providing two key advantages. First, EBSs robustly mitigate grid cell-crossing errors by offering continuous gradients of the basis functions on the interface between adjacent grid cells. Second, numerical integration errors are minimised, even with small physical domains in occupied grid cells. The proposed method's robustness and accuracy are evaluated through benchmarks, including comparisons with analytical solutions, other state-of-the-art MPM-based contact algorithms, and experimental observations from the literature. Notably, the method demonstrates effective mitigation of stress errors inherent in contact simulations.

1 | Introduction

Robust numerical modelling of contact problems is crucial for various engineering applications, including tyre-road interaction [1], soil-structure interaction [2, 3], and metal forming [4] amongst many. Despite significant progress in improving the accuracy of numerical simulations in contact mechanics, capturing the kinematic response of solid bodies during contact or impact remains a challenging task [5, 6].

Errors in stress predictions become more pronounced when dealing with deformable bodies of complex geometries in contact or impact scenarios. Mesh-based simulation methods (e.g., [7–10]) can treat contact, even in large deformations, when the mesh distortion error is not severe [11, 12]. However, the fidelity of the simulation rapidly deteriorates due to mesh distortion. To address this, various numerical remedies have been proposed, such as re-meshing, though requiring additional computational time [13].

The Material Point Method (MPM) [14] is a robust approach for solving contact problems by discretising the continuum into Lagrangian material points. These points carry properties such as mass, position, velocity, and stress. Unlike purely meshless methods, MPM employs a background Eulerian grid (computational mesh) for calculating forces and momentum. With its Eulerian–Lagrangian formulation, MPM delivers high-fidelity solutions for domains undergoing large deformations [15, 16].

Notably, MPM excels in contact mechanics problems, enabling the straightforward detection of contact surfaces [17–24]. However, the MPM has been reported to face three main challenges, which yield severe stress errors ("noise") at the contact surface, that is, errors arising from premature contact detection (early contact), grid cell-crossing errors, and errors arising in stresses due to incomplete numerical integration over boundary grid cells when these are occupied by a small physical domain. In this work, we introduce a novel MPM variant that leverages the merits of the Extended B-Spline (EBS) MPM [25] and reformulates it within a penalty function contact setting inspired by [26] to simultaneously treat these errors.

Early contact errors refer to the premature contact stresses arising between material points, that is, before the physical domains actually come into contact, see, for example, [27]. This aspect has been treated using penalty methods, starting from the seminal work of [26]. In [28], the penalty method has been combined with a level-set representation of the boundary surfaces to increase accuracy. Building on the penalty contact method initially introduced by Zavarise and Wriggers in [29] within a finite element setting, Guilkey et al. [24, 30] proposed a penalty contact method for the MPM where the physical boundary is discretised into line segments (in 2D) or triangulated surfaces (in 3D). In this approach, the contact forces are projected from the discretised contact area back to the Eulerian grid, where the governing equations are solved. Although this implementation provides more accurate estimates of the contact problem, the domain has to be discretised sufficiently fine to approximate a solution region accurately. Very recently [31], introduced an MPM method that resides on a Discrete Element Method (DEM) formulation to treat multi-material interactions.

An alternative approach to penalty methods has been proposed in [21] where logistic regression was employed to estimate the contact surface normal vector and to define the domain boundaries. As already explained in [24], logistic regression may struggle in scenarios featuring small deformations between stiff objects. In such cases, including scenarios with curved surfaces, the method, along with its predecessors, tends to overestimate the contact area, consequently leading to an underestimation of stress in contact regions. To further verify this issue, the logistic regression approach is compared with the proposed contact algorithm in the numerical examples presented in this study.

In this work, the solid body boundaries are represented by introducing additional material points, termed boundary material points. Those boundary material points have both mass and volume contributions to the solid body they belong to and are treated in a similar manner to the material points in the bulk. Thus, no special treatment is required to update their properties, that is, position, velocity, and so forth. Contact forces arise when a material point along the boundary of one solid body penetrates a segment defined by material points along the boundary of another solid body. This approach is conceptually similar to the virtual slave node technique described by Zavarise et al. [32], which improves the transfer of forces and contact pressures at the slave surface nodes. Unlike traditional finite element-based methods that compute contact forces at discrete nodes, leading to inaccuracies due to the discrete representation of the slave surface, the virtual slave node technique introduces additional computational points-typically at Gauss or quarter points-within the slave element. In contrast, this work evenly distributes boundary material points along the solid boundary, ensuring that each segment contains at least two boundary material points (in 2D). This approach enhances the contact force distribution.

Grid cell-crossing errors occur when material points cross grid cell boundaries due to non-continuous gradients of the basis functions. To this point, several methods have been introduced to treat this, starting from the Generalised Interpolation Material Point (GIMP), see, for example, [33, 34], the Convected Material Point Domain Interpolation (CPDI), see, for example, [35, 36], the Second-order CPDI (CPDI2), see, for example, [37], the Total Lagrangian Material Point Method (TLMPM) [23], the C_0 enhancement scheme [38], and the Staggered Grid MPM (SGMP) [39]. The CPDI is one of the most accurate variants of the GIMP to date. In CPDI, the shape functions of the background grid are replaced with shape functions defined within each material point's domain, typically assumed to be a parallelogram whose edges require tracking [37].

In comparison, B-Spline basis functions are highly effective in mitigating the cell-crossing instability, without the requirement of additional algorithmic manipulations. B-splines are directly employed at the background grid cells and resolve grid cell crossing by providing increased continuity at the interface. The merits of using a higher-order continuity basis in the MPM have been extensively examined in the literature; see, for example, [40, 41]. In this work, we adopt this remedy because of its favourable characteristics. We employ an EBS interpolation scheme that in addition to providing higher order continuity, can minimise numerical integration errors, even when boundary grid cells are occupied by small physical domains. To further highlight the advantages of EBS over state-of-the-art methods, such as CPDI approximations, the proposed penalty contact algorithm is also applied to the widely used CPDI2 scheme [37].

Numerical integration errors refer to stress errors arising from the incomplete integration over boundary grid cells when occupied by a small physical domain. This occurs when material points occupy a region much smaller than the grid cell. Mitigating this involves techniques such as the "cut-off" method proposed by [42], which introduces a model parameter, but it imposes undesirable constraints. Other approaches include the momentum formulation of the MPM [42] and the Modified Update Stress Last (MUSL) approach [43], both adopted in this work (detailed in Section 3).

The EBS method was first introduced by Yamaguchi et al. [25] within a MPM framework, demonstrating its ability to mitigate integration errors. Due to its advantages, EBS-MPM has attracted interest from the research community and has been successfully applied to model large deformations, particularly for nearly incompressible materials, using an advanced stabilised MPM approach [44, 45]. However, its potential in contact mechanics remains largely unexplored. This study aims to fill this gap by introducing the EBS within a penalty-based contact numerical framework. Additionally, our approach incorporates boundary material points to accurately capture the physical boundary of the deformable domain and the evolving contact stresses. Unlike the method presented by Guilkey et al. [24], our boundary material points are physical points that have mass, thereby influencing the stress distribution within the domain. Benchmark tests are conducted to verify the effectiveness of the proposed algorithm, with numerical results compared against analytical solutions and state-of-the-art MPM contact models from the literature.

The manuscript is organised as follows: Section 2 introduces the governing equations for frictional contact problems. Subsequently, Section 3 delves into the EBSs-based MPM discretisation scheme and its numerical implementation. Section 4 presents numerical examples to verify and validate the proposed method, comparing its efficiency with analytical solutions, other contact algorithms, and experimental observations. Finally, Section 5 offers concluding remarks and outlines future directions.

2 | Governing Equations for Frictional Contact

2.1 | Principal Balance of Energy

This section briefly discusses the case of two bodies in contact, as illustrated in Figure 1. The method is naturally extendable to handle multiple domains in contact, as demonstrated in Section 4. The study focuses on a deformable domain Ω with an outer boundary $\partial\Omega = \partial\Omega_1 \cup \partial\Omega_2$, comprising two bodies denoted as discrete fields, namely Ω_1 (master) and Ω_2 (slave). Here, $\Omega = \Omega_1 \cup \Omega_2 \subset \mathbb{R}^d$ with $d \in 1, 2, 3$. At time t, the deformable bodies are assumed to be in contact along a contact surface $\partial\Omega_{\bar{\mathbf{f}}}$, as shown in Figure 1a. The normal and tangential contact vectors are denoted by $\bar{\mathbf{f}}_1^{nor} = -\bar{\mathbf{f}}_2^{nor}$ and $\bar{\mathbf{f}}_1^{tan} = -\bar{\mathbf{f}}_2^{tan}$, respectively, with their magnitudes represented as $\bar{\mathbf{f}}_1^{cont} = -\bar{\mathbf{f}}_2^{cont}$.

Assuming contact violation, where one discrete field penetrates another in the region $\partial\Omega_{\bar{\mathbf{f}}}$, the total energy of domain Ω is penalised using a proportional penalty governed by the function $\mathcal{P}$. This penalty function is expressed as:

$$\mathcal{P}(\mathbf{u}) = \frac{1}{2}\omega^{nor}\int_{\partial\Omega_{\bar{\mathbf{f}}}} (g^{nor})^2 d\partial\Omega_{\bar{\mathbf{f}}} + \frac{1}{2}\omega^{tan}\int_{\partial\Omega_{\bar{\mathbf{f}}}} \left(g^{tan}\right)^2 d\partial\Omega_{\bar{\mathbf{f}}} \tag{1}$$

Here, ω is a large penalty parameter, g^{nor} is the normal gap function, and g^{tan} is the tangential slip function. The superscripts $(\cdot)^{nor}$ and $(\cdot)^{tan}$ denote the normal and tangential directions, respectively.

The normal gap and tangential slip functions, following [26], depend on the relative distance between a slave point, s, on $\partial\Omega_{2\bar{\mathbf{f}}} \subset \partial\Omega_2$, and its projection onto the master segment of $\partial\Omega_{1\bar{\mathbf{f}}} \subset \partial\Omega_1$. The symbols $\partial\Omega_{1\bar{\mathbf{f}}}$ and $\partial\Omega_{2\bar{\mathbf{f}}}$ represent the contact surfaces of Ω_1 and Ω_2, respectively.

Remark 1. The formulation in Equation (1) quantifies the extent of constraint violation by employing a penalty coefficient that scales with the constraint error. Detailed information about the gap and slip functions used in this context is available in Section 3.6.

It follows from Equation (1) that the rate of the penalty function can be written as

$$\dot{\mathcal{P}}(\dot{\mathbf{u}}) = \omega^{nor}\int_{\partial\Omega_{\bar{\mathbf{f}}}} (\dot{g}^{nor}) d\partial\Omega_{\bar{\mathbf{f}}} + \omega^{tan}\int_{\partial\Omega_{\bar{\mathbf{f}}}} \left(\dot{g}^{tan}\right) d\partial\Omega_{\bar{\mathbf{f}}} \tag{2}$$

Hence, the total energy of the system is expressed as

$$\mathcal{T}(\mathbf{u}) = \mathcal{K}(\mathbf{u}) + \mathcal{W}^{int}(\mathbf{u}) - \mathcal{W}^{ext}(\mathbf{u}) + \mathcal{P}(\mathbf{u}) \tag{3}$$

where $\mathcal{K}$, $\mathcal{W}^{int}$ and $\mathcal{W}^{ext}$ are the total kinetic energy, the internal work, and the external work to the system, respectively [46]. The symbol $\mathbf{u} = \mathbf{u}(\mathbf{x}, t)$ denotes the displacement of a point $\mathbf{x} = \{x_1, x_2, x_3\}$ at time t. Employing the principle of balance of energy, the strong form for frictional contact is derived as

$$\dot{\mathcal{T}}(\dot{\mathbf{u}}) = \dot{\mathcal{K}}(\dot{\mathbf{u}}) + \dot{\mathcal{W}}^{int}(\dot{\mathbf{u}}) - \dot{\mathcal{W}}^{ext}(\dot{\mathbf{u}}) + \dot{\mathcal{P}}(\dot{\mathbf{u}}) = 0 \tag{4}$$

where the symbol $(\dot{\cdot})$ denotes differentiation with respect to time.

2.2 | Strong Form

Applying the divergence theorem in Equation (4), performing the necessary algebraic manipulations, and finally considering

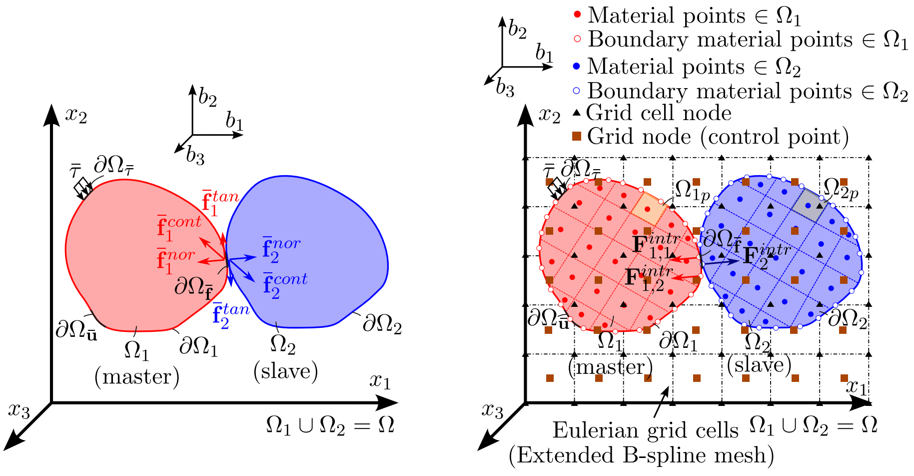

(a)

(b)

FIGURE 1 | (a) Continuum bodies (discrete fields) into contact and (b) material point method approximation.

that the resulting expression must hold for arbitrary values of $\dot{\mathbf{u}}$, dynamic equilibrium is established as

$$\nabla \cdot \boldsymbol{\sigma} + \mathbf{b} = \rho \ddot{\mathbf{u}} \qquad \text{on } \Omega \tag{5}$$

where $\boldsymbol{\sigma} = \partial \psi_{el} / \partial \boldsymbol{\varepsilon}$ is the stress field and $\psi_{el}(\boldsymbol{\varepsilon})$ is the elastic energy density. In this work, linear elastic materials are considered, and hence the strain tensor, $\boldsymbol{\varepsilon}$ is expressed as

$$\boldsymbol{\varepsilon} = \frac{1}{2}\left(\nabla \mathbf{u} + \nabla \mathbf{u}^T\right) \tag{6}$$

according to the infinitesimal strain theory [47]; the (∇) stands for the gradient operator. In Equation (5), $\mathbf{b} = \{b_1, b_2, b_3\}$ are the body forces, ρ the mass density, and $\ddot{\mathbf{u}} = d\mathbf{u}/dt$ the acceleration field.

Equation (5) is also subjected to the set of boundary and initial conditions defined in Equation (7)

$$\begin{cases} \boldsymbol{\sigma} \cdot \mathbf{n} = \bar{\boldsymbol{\tau}}, & \text{on } \partial\Omega_{\bar{\boldsymbol{\tau}}} \\ \bar{\mathbf{f}}^{nor} = -\omega_{nor} g^{nor} \mathbf{e}^{nor}, & \text{on } \partial\Omega_{\bar{\mathbf{f}}} \\ \bar{\mathbf{f}}^{tan} = -\omega_{tan} g^{tan} \mathbf{e}^{tan}, & \text{on } \partial\Omega_{\bar{\mathbf{f}}} \\ \mathbf{u} = \bar{\mathbf{u}}, & \text{on } \partial\Omega_{\bar{\mathbf{u}}} \\ \mathbf{u} = {}^{(0)}\mathbf{u}, & \text{on } {}^{(0)}\Omega \\ \dot{\mathbf{u}} = {}^{(0)}\dot{\mathbf{u}}, & \text{on } {}^{(0)}\Omega \\ \ddot{\mathbf{u}} = {}^{(0)}\ddot{\mathbf{u}}, & \text{on } {}^{(0)}\Omega \end{cases} \tag{7}$$

where $\mathbf{n}$ is the outward unit normal vector of the boundary, $\bar{\mathbf{u}}$ are the prescribed displacements on $\partial\Omega_{\bar{\mathbf{u}}}$, and $\bar{\boldsymbol{\tau}}$ corresponds to the set of traction forces at $\partial\Omega_{\bar{\boldsymbol{\tau}}}$. Symbols $\mathbf{e}^{nor}$ and $\mathbf{e}^{tan}$ denote the normal and tangential unit vectors, respectively. The notation ${}^{(t)}(\cdot)$ indicates the quantity $(\cdot)$ at time t. Herein, symbols ${}^{(0)}\mathbf{u}$, ${}^{(0)}\dot{\mathbf{u}}$, and ${}^{(0)}\ddot{\mathbf{u}}$ are the initial displacement, velocity, and acceleration field, respectively, at initial solid configuration ${}^{(0)}\Omega$.

Furthermore, the strong form, Equation (5) is subjected to the kinematic constraints presented in Equations (8a)–(8e) and (9a)–(9e) at the contact surface $\partial\Omega_{\bar{\mathbf{f}}}$ [46].

The kinematic constraints of Equations (8a)–(8e) correspond to the normal contact laws

$$\begin{cases} \mathbf{e}_1^{nor} = -\mathbf{e}_2^{nor}, & \text{Collinearity,} & \text{on } \partial\Omega_{\bar{\mathbf{f}}} & \text{(8a)} \\ \bar{\mathbf{f}}_1^{nor} = -\bar{\mathbf{f}}_2^{nor}, & \text{Collinearity,} & \text{on } \partial\Omega_{\bar{\mathbf{f}}} & \text{(8b)} \\ \bar{f}^{nor} \leq 0, & \text{Non-tension,} & \text{on } \partial\Omega_{\bar{\mathbf{f}}} & \text{(8c)} \\ g^{nor} \geq 0, & \text{Impenetrability,} & \text{on } \partial\Omega_{\bar{\mathbf{f}}} & \text{(8d)} \\ g^{nor} \bar{f}^{nor} = 0, & \text{Complementarity,} & \text{on } \partial\Omega_{\bar{\mathbf{f}}} & \text{(8e)} \end{cases}$$

whereas Equations (9a)–(9e) correspond to the tangential contact and friction laws, where the Coulomb friction model is adopted.

$$\begin{cases} \mathbf{e}_1^{tan} = -\mathbf{e}_2^{tan}, & \text{Collinearity,} & \text{on } \partial\Omega_{\bar{\mathbf{f}}} & \text{(9a)} \\ \bar{\mathbf{f}}_1^{tan} = -\bar{\mathbf{f}}_2^{tan}, & \text{Collinearity,} & \text{on } \partial\Omega_{\bar{\mathbf{f}}} & \text{(9b)} \\ |\bar{f}^{tan}| \leq \mu_f |\bar{f}^{nor}|, & \text{Coulomb friction,} & \text{on } \partial\Omega_{\bar{\mathbf{f}}} & \text{(9c)} \\ |g^{tan}| \geq 0, & \text{Slip/Non-Slip,} & \text{on } \partial\Omega_{\bar{\mathbf{f}}} & \text{(9d)} \\ |g^{tan}| \left(|\bar{f}^{tan}| - \mu_f |\bar{f}^{nor}|\right) = 0, & \text{Complementarity,} & \text{on } \partial\Omega_{\bar{\mathbf{f}}} & \text{(9e)} \end{cases}$$

The Karush–Kuhn–Tucker (KKT) conditions Equations (8a)–(9e) enforce normal and tangential contact laws at the boundary $\partial\Omega_{\bar{\mathbf{f}}}$. These constraints, illustrated in Figure 1, uphold Newton's third law at the contact surface. The non-tension condition Equation (8c) ensures non-stick contact.

Additionally, impenetrability condition Equation (8d) prevents penetration between $\partial\Omega_{1\bar{\mathbf{f}}}$ and $\partial\Omega_{2\bar{\mathbf{f}}}$ when in contact. The Coulomb friction model in Equation (9c) governs the tangential component $\overline{f}^{tan}$, related to slip contact. The condition $|g^{tan}| = 0$ denotes no slip, while $|g^{tan}| > 0$ indicates slip, satisfying $|\overline{f}^{tan}| = \mu_f |\overline{f}^{nor}|$. Regularisation through penalty parameters ω^{nor} and ω^{tan} weakly imposes these constraints. The green dashed line in Figure 2a,b represents this weak enforcement, addressing potential zig-zagging in the tangential direction. For further details, refer to [28, 48]. Section 3.6 elaborates on gap functions, slip functions, and contact force evaluation.

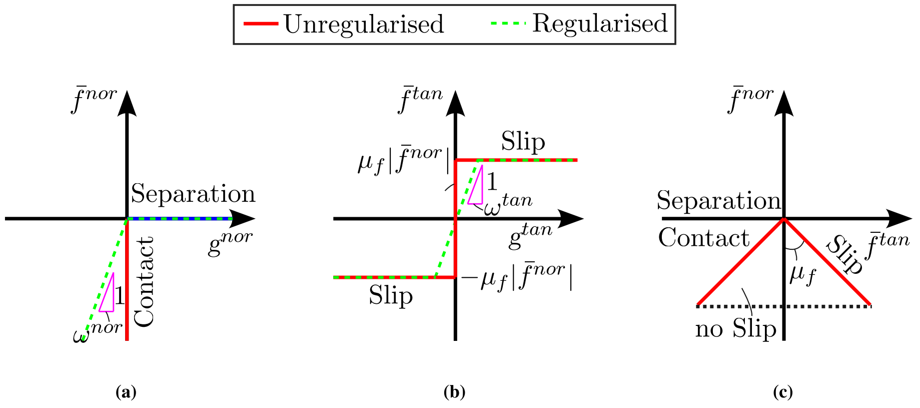

(a) (b) (c)

FIGURE 2 | Kinematic contact constraints. (a) Normal contact law, (b) tangential contact law, and (c) Coulomb's cone for the two-dimensional problem. As a result of employing a penalty function approach and incorporating the penalty parameters ω^{nor} and ω^{tan}, kinematic constraints are "weakly" imposed, as illustrated by a dashed green line.

3 | An Extended B-Spline MPM for Frictional Contact

3.1 | MPM Approximation

This work employs the MPM to discretise the governing equations (5). The domain $\Omega = \Omega_1 \cup \Omega_2$ is discretised into material points $\mathcal{Q} = p | p = 1, 2, \dots, n_p$. Let n_{Dp} be the number of material points in discrete field $\mathcal{D}$ (e.g., Ω_D). For two solid bodies, $n_p = n_{1p} + n_{2p}$. Figure 1b illustrates the MPM for two separate discrete fields (master in red, slave in blue).

In MPM, mass density ρ_D and domain volume Ω_D for discrete field $\mathcal{D}$ decompose into material point contributions per Equations (10) and (11):

$$\rho_D(\mathbf{x}_D, t) = \sum_{p=1}^{n_p} \rho_{Dp}\Omega_{Dp}\delta(\mathbf{x}_D - \mathbf{x}_{Dp}) \tag{10}$$

and

$$\Omega_D(\mathbf{x}_D, t) = \sum_{p=1}^{n_p} \Omega_{Dp}\delta(\mathbf{x}_D - \mathbf{x}_{Dp}) \tag{11}$$

Here, $\mathbf{x}_D$ is the position vector of discrete field $\mathcal{D}$, and δ is the Dirac delta function. The material point mass density is $\rho_{Dp} = M_{Dp}/\Omega_{Dp}$, where M_{Dp} and Ω_{Dp} and are the material point mass and volume, respectively. The symbol $(\cdot)_{Dp}$ denotes a quantity of material point p at discrete field $\mathcal{D}$. Lagrangian material points move within a fixed Eulerian grid, consisting of n_n grid nodes and n_{cells} grid cells (Figure 1b).

3.2 | Discrete Equilibrium Equations

The discrete equilibrium equations (5) are expressed for each discrete field $\mathcal{D}$ as

$$\mathbf{M}_D\ddot{\mathbf{u}}_D + \mathbf{F}_D^{int} = \mathbf{F}_D^{ext} + \mathbf{F}_D^{cont} \tag{12}$$

with the last term representing externally applied contact forces. The lumped mass matrix $\mathbf{M}_D$ is defined as

$$M_{DI} = \sum_{p=1}^{n_p} \left(\rho_{Dp}N_I(\mathbf{x}_p)\right)\Omega_{Dp} \tag{13}$$

where $N_I(\mathbf{x}_p)$ are the interpolation functions evaluated at the material points.

The nodal components of inertia forces $\mathbf{F}_{DI}^{irt}$ and internal forces $\mathbf{F}_{DI}^{int}$ are expressed as

$$\mathbf{F}_{DI}^{irt} = \sum_{p=1}^{n_p}(\rho_{Dp}\ddot{\mathbf{u}}_{Dp} \cdot N_I(\mathbf{x}_p))\Omega_{Dp} \tag{14}$$

and

$$\mathbf{F}_{DI}^{int} = \sum_{p=1}^{n_p}(\boldsymbol{\sigma}_{Dp} \cdot \nabla N_I(\mathbf{x}_p))\Omega_{Dp} \tag{15}$$

respectively, where $\nabla N_I(\mathbf{x}_p)$ are the interpolation functions spatial derivatives.

The nodal components of the external force vector $\mathbf{F}_{DI}^{ext}$ are computed as

$$\mathbf{F}_{DI}^{ext} = \int_{\partial\Omega_{\bar{\tau}}} (\bar{\boldsymbol{\tau}} N_I(\mathbf{x}))\, d\partial\Omega_{D\bar{\tau}} + \sum_{p=1}^{n_p} \mathbf{b}_p N_I(\mathbf{x}_p)\Omega_{Dp} \tag{16}$$

The contact force nodal vector $\mathbf{F}_{DI}^{cont}$ is defined as

$$\mathbf{F}_{DI}^{cont} = \int_{\partial\Omega_{D\bar{\mathbf{f}}}} (\bar{\mathbf{f}}_D^{cont} N_I(\mathbf{x}))\, d\partial\Omega_{D\bar{\mathbf{f}}} \tag{17}$$

The acceleration field is interpolated in a Galerkin sense as

$$\ddot{\mathbf{u}}_{Dp} = \sum_{I=1}^{n_n} N_I(\mathbf{x}_p)\ddot{\mathbf{u}}_{DI} \tag{18}$$

where $\ddot{\mathbf{u}}_{DI}$ represents the components of the nodal acceleration vector at node I. Displacement and velocity fields are derived similarly. Equation (12) can be adapted to an explicit time integration scheme, as detailed in Section 3.7.

3.3 | Computational Grid Interpolation Functions

In this study, the mapping between material points and grid nodes is achieved using EBS interpolation functions, discussed in Section 3.3.1. These functions are derived from the standard B-Splines (referred to as Original B-Splines, or OBSs, in this work). Definition of the OBSs can be found in [49, 50].

3.3.1 | Extended B-Spline Interpolation Functions

In this study, the approach from [25] is adopted, leveraging OBS functions to minimise grid cell crossing errors, with EBS activated in boundary grid cells. EBS is crucial to mitigate stress errors arising from numerical integration issues in boundary cells. This is demonstrated in the numerical examples in Section 4. This section briefly discusses the EBS implementation to facilitate understanding of the classification of the basis functions as well as how EBS is fitted into frictional contact problems with MPM. The evaluation of EBSs involves a three-step procedure.

Step 1: Calculation of the Volume Fraction

The initial step computes the grid cell volume fraction (ϕ_c), representing the ratio of the total material point volume in a specific boundary grid cell to the cell's volume:

$$\phi_c = \frac{\sum_{p\in\mathcal{O}} \Omega_p}{\Omega_c} \tag{19}$$

Step 2: Classification of the Grid Cells

Next, grid cells are classified as interior, boundary, or exterior based on the volume fraction:

$$\text{Grid cell is categorised as} \begin{cases} \text{interior} & \text{if} \quad \phi_c > C_c \\ \text{boundary} & \text{if} \quad 0 < \phi_c \leq C_c \\ \text{exterior} & \text{if} \quad \phi_c = 0 \end{cases} \tag{20}$$

where C_c is the *occupation parameter*.

Step 3: Classification of Basis Functions

The final step involves classifying B-Spline basis functions into stable, degenerate, and exterior groups:

- **Stable:** if $\mathrm{supp}(N_I)$ contains at least one interior grid cell.
- **Degenerated:** if $\mathrm{supp}(N_I)$ contains no interior and at least one boundary grid cell.
- **Exterior:** if otherwise.

This classification ensures a robust representation of basis functions, addressing issues related to ill-conditioned matrices and non-uniform distribution of material points during large deformations. For more details, refer to [25].

In Figure 3, a visual representation depicts the categorised bases, grid cells, and nodes using two-dimensional quadratic EBSs basis functions.

The stable and degenerated B-Splines, whose associated nodes are denoted by $\mathbb{I}$ and $\mathbb{J}$, respectively, are used to approximate the function near the boundary of a physical domain. The displacement field approximation is rewritten as

$$\mathbf{u}_{Dp} = \sum_{I\in\mathbb{I}} N_I(\mathbf{x}_p)\mathbf{u}_{DI} + \sum_{J\in\mathbb{J}} N_J(\mathbf{x}_p)\mathbf{u}_{DJ} \tag{21}$$

Similar expressions are established for the velocity and acceleration fields. The coefficients of the degenerated bases are replaced by the linear combination of those of the stable bases as

$$\mathbf{u}_J = \sum_{I\in\mathbb{I}_J} E_{IJ}\mathbf{u}_I \tag{22}$$

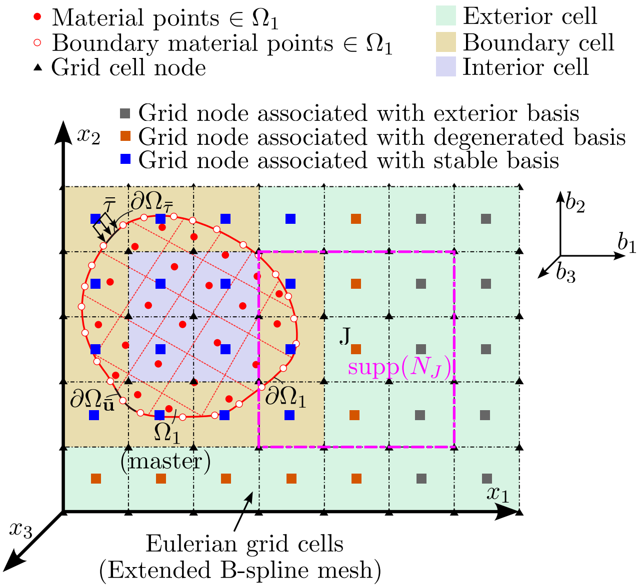

FIGURE 3 | Categorising grid cells and nodes with classified bases on a two-dimensional continuum covered by an Eulerian grid. This is made according to the value of the volume fraction, ϕ_c, at the boundary grid cells in relation to the occupation parameter, C_c, chosen for the simulation.

where E_{IJ} are the values of Lagrange polynomials at grid node J for extrapolating the value of $\mathbf{u}$ at $J \in \mathbb{J}$ by using nodal values $\mathbf{u}_I$ with $I \in \mathbb{I}$. $\mathbb{I}_J \subseteq \mathbb{I}$ is a set of grid nodes associated with stable bases adjacent to grid node J. As already presented in [25], E_{IJ} can be expressed as

$$E_{IJ} = \prod_{a=1}^{d}\left(\prod_{\chi=0,\chi\neq I^a-\kappa_J^a}^{q_\xi} \frac{J^a-\kappa_J^a-\chi}{I^a-\kappa_J^a-\chi}\right) \tag{23}$$

when uniform knot vectors are used. The symbol, κ, denotes a starting point such as $\mathbb{I}_J = \kappa + [0,\ldots,q_\xi]^d$. This is also illustrated in the one-dimensional example in Figure 4.

The substitution of Equation (23) into (22) and then into Equation (21) yields the following expression for interpolation

$$\mathbf{u}_{Dp} = \sum_{I\in\mathbb{I}} N_I^{ebs}(\mathbf{x}_p)\mathbf{u}_{DI} \tag{24}$$

The EBS interpolation functions are eventually defined as

$$N_I^{ebs}(\mathbf{x}_p) = N_I(\mathbf{x}_p) + \sum_{J\in\mathbb{J}_I} N_J(\mathbf{x}_p)E_{IJ} \tag{25}$$

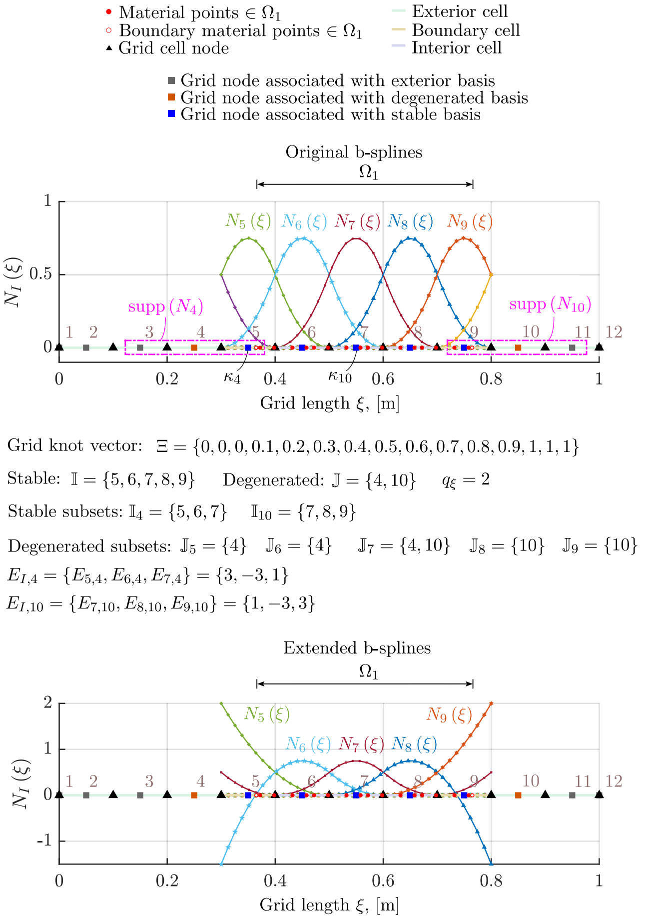

FIGURE 4 | Derivation of quadratic Extended B-Splines from the original B-Splines for the case of a one-dimensional Eulerian grid. In this example, an occupation parameter at $C_c = 0.75$ is utilised. Grid cells with identities, 4 and 8, are marked as boundary grid cells, resulting in two degenerated basis functions, associated with grid nodes (control points) 4 and 10.

where $\mathbb{J}_I$ is the reciprocal set to $\mathbb{I}_J$. The first derivatives of the EBSs are expressed accordingly as

$$\nabla N_I^{ebs}(\mathbf{x}_p) = \nabla N_I(\mathbf{x}_p) + \sum_{J \in \mathbb{J}_I} \nabla N_J(\mathbf{x}_p) E_{IJ} \tag{26}$$

Figure 4 illustrates the derivation of quadratic EBSs from the Original B-Splines (OBSs) for the case of one-dimensional example. In this example, an occupation parameter, $C_c = 0.75$, is utilised.

3.4 | Domain Boundary Representation

In this work, solid body boundaries are represented by introducing additional material points, termed boundary material points. These points, depicted as “unfilled” circles in figures, for example, Figures 1b and 3, serve to delineate the solid body boundaries. The total volume and mass of boundary material points are set to 0.1% of the domain's total volume and mass, respectively, in the numerical tests. The boundary material points are positioned at the centre of their corresponding material point domains. Connecting these boundary material points with linear segments, as demonstrated in Section 4, yields good results. Although alternative boundary representations exist, such as those employing higher-order B-Splines [40], they are beyond the scope of this work.

In the present work, the boundary material points are treated in a similar manner to the material points in the bulk; hence, no special treatment is required to update their properties, that is, position, velocity, and so forth. The velocities of both the bulk and the boundary material points are projected onto the Eulerian grid to obtain the nodal values and solve the governing equations at grid nodes. The numerical implementation is detailed in Section 3.7.

In comparison [24], represented the boundary of the domain by defining a set of vertices—either line segments connected end to end in two dimensions or triangles in three dimensions. Regardless of dimensionality, these elements are massless and are advected using the velocity field of the associated material. However, special treatment is required for the massless elements at the domain boundary to follow bulk deformation when grid nodes with a non-zero value of the basis function have undefined velocity values. In particular, the velocities of the bulk material points are initially projected onto the Eulerian grid to obtain the nodal velocities. Next, the nodal velocities are updated and then are projected to the vertices that form the domain boundary. Vertices properties are updated utilising their velocity values. Although this process yields accurate estimates for contact problems, it necessitates more computational time compared to the present approach, which updates the boundary material points in a more natural manner.

3.5 | Boundary Tracking

Boundary tracking, the process of identifying contact surfaces or points, is achieved in this work through a slave point—master segment pairing. The slave point is any boundary material point within the slave discrete field, while the master segment refers to a segment formed by consecutive boundary material points in the master discrete field.

This contact pair detection involves a three-step process:

1. **Common control points detection:** Check if boundary material points from different fields contribute to the same control point by projecting material point volumes to grid nodes using Equation (27)

$$\Omega_{DI} = \sum_{p=1}^{n_p} \left(N_I(\mathbf{x}_p) \Omega_{Dp} \right) \tag{27}$$

   Shared control points indicate potential contact zones. For example, Ω_1 and Ω_2 share the same grid node I when $\Omega_{1I} > 0$ and $\Omega_{2I} > 0$ simultaneously.
2. **Distance check:** Examine if the distance between boundary material points from different fields is less than a minimum search size, typically the computational grid spacing denoted as Δh.
3. **Contact pair determination:** Establish a slave boundary material point—master segment pair by verifying if $g^{nor} < 0$. This condition ensures the penetration of the slave boundary material point into the master segment. Figures 5 and 6 provide a visual representation of such pairs.

The process described above results in great computational gains since detection of the slave-master segment pair is restricted to specific areas. This is a merit of the proposed method in comparison to other MPM contact implementations, such as [24], which require massive intersection detection between the geometry components at each time step.

3.6 | Definition of the Gap Functions and Contact Forces Evaluation

To enforce contact constraints and prevent object penetration, a gap function measures the Euclidean distance between the boundaries of potentially contacting objects. This work adopts the normal gap and tangential slip functions introduced in [26], which are expressed as

$$^{(t)}g^{nor} = \left({}^{(t)}\mathbf{x}_s - {}^{(t)}\mathbf{x}_{\bar{s}} \right) \cdot {}^{(t)}\mathbf{e}^{nor^T} \qquad \text{on } \partial\Omega_{\bar{\mathbf{f}}} \tag{28}$$

and

$$^{(t)}g^{tan} = {}^{(t-\Delta t)}l_{ms} \left({}^{(t)}\beta_{\bar{s}} - {}^{(t-\Delta t)}\beta_{\bar{s}} \right) \qquad \text{on } \partial\Omega_{\bar{\mathbf{f}}} \tag{29}$$

respectively. The symbol l_{ms} denotes the length of the master segment while Δt is the time step.

In Equation (28), $\mathbf{x}_s$ denotes the position vector of the slave node s, and $\mathbf{x}_{\bar{s}}$ is the position vector of s projected onto the master segment. The normal gap function, g^{nor}, measures the Euclidean distance between the slave node s and its projection $\bar{s}$ on the master segment. As discussed in Section 2.2, $g^{nor} > 0$ holds when the bodies are not in contact (see Figure 6a), and $g^{nor} < 0$ when the slave body penetrates the master body (see Figure 6b, c). In Figure 6,

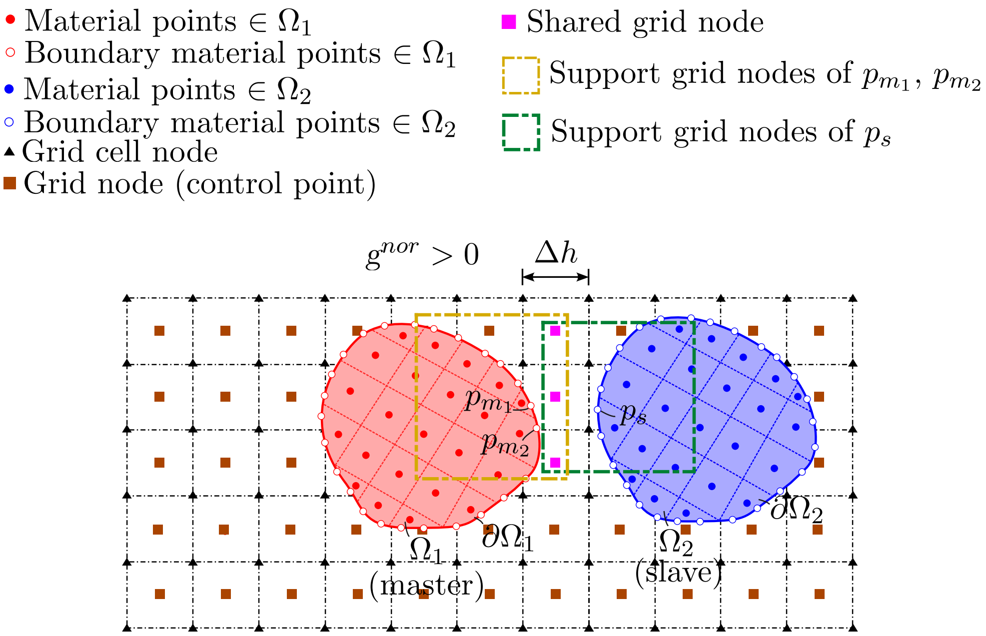

FIGURE 5 | Boundary tracking process. Step 1: shared control points indicate potential contact zones. Step 2: distance of the boundary materials points is less than the grid spacing, Δh. Step 3: the $g^{nor} > 0$, which indicates that the slave material point p_s is not in contact with the master segment, formed by boundary material points p_{m_1} and p_{m_2}.

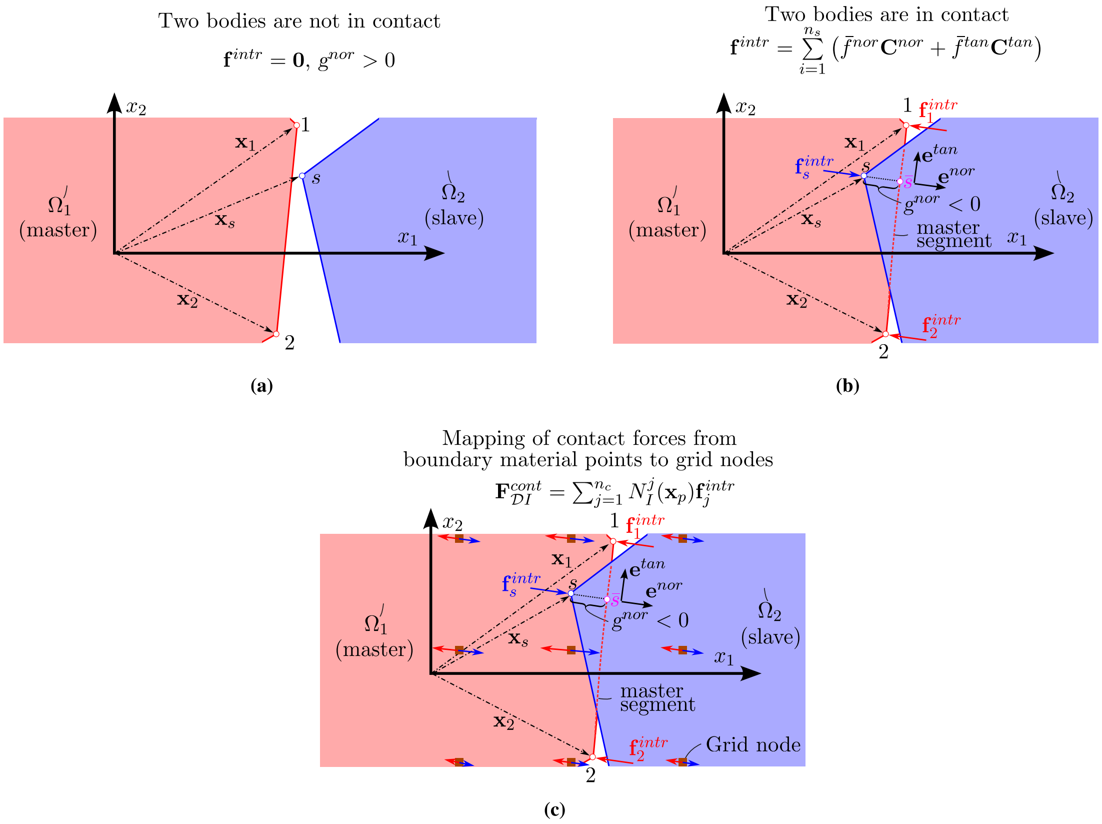

FIGURE 6 | (a) Two bodies are not in contact. There are no interaction forces between the two bodies, and the normal gap function $g^{nor} > 0$; (b) two bodies are in contact. There are interaction forces between the two bodies. The slave boundary material point has penetrated the master segment, and (c) mapping of contact forces from material points to grid nodes. Then, the grid nodal contact forces are added to the grid nodal governing equations of motion (see Equation (12)) that are updated.

note that $\mathbf{e}^{nor}$ represents the unit outwards normal vector at the contact surface, starting from $\mathbf{x}_s$ and ending at $\mathbf{x}_{\bar{s}}$.

In Equation (29) and for the tangential direction, $\mathbf{x}_1$ indicates the position vector of one end of the master segment. As also presented in Figure 6, position vectors $\mathbf{x}_1$ and $\mathbf{x}_2$ form the two ends of the master segment. The symbol, β, denotes the natural coordinate of $\bar{s}$ on the master segment, and it is expressed as

$$ {}^{(t)}\beta_{\bar{s}} = \frac{1}{{}^{(t)}l_{ms}} \left({}^{(t)}\mathbf{x}_{\bar{s}} - {}^{(t)}\mathbf{x}_1 \right)^T \cdot {}^{(t)}\mathbf{e}^{tan} \qquad \text{and} \qquad 0 < \beta < 1 \tag{30} $$

The tangential slip function measures the amount of relative movement of the two contact surfaces, $\partial\Omega_{1\bar{\mathbf{f}}}$ and $\partial\Omega_{2\bar{\mathbf{f}}}$, within a time increment. A graphical representation of the tangential slip is illustrated in Figure 7 for two time steps, that is, (a) $t - \Delta t$ and (b) t.

When the two bodies are in contact (see Figure 6b), the normal contact component is evaluated from the Equation (31)

$$ {}^{(t)}\overline{f}^{nor} = \omega^{nor\,(t)}\mathrm{g}^{nor} \tag{31} $$

while the corresponding tangential component from Equation (32)

$$ {}^{(t)}\overline{f}^{tan} = \min\left(\mu_f \left|\overline{f}^{nor}\right|, \omega^{tan} \left|{}^{(t)}\mathrm{g}^{tan}\right| \right) \operatorname{sign}(-{}^{(t)}\mathrm{g}^{tan}) \tag{32} $$

Remark 2. In this work, an isotropic Coulomb friction model has been adopted to facilitate a direct comparison of the proposed method with other MPM variants in standard benchmark tests. Investigating more involved contact laws is beyond the scope of this research. We note, however that an alternative friction contact law may be applied within the context of the proposed method by revisiting the definitions of the normal gap and tangential slip functions and the tangential contact force component. The interested reader can refer to, for example, [22, 30], for further insights. In addition, because boundary material points are treated in the same manner as the material points in the bulk, the proposed method has the potential to accommodate history-dependent contact laws. Previous research has developed MPM contact algorithms incorporating history-dependent contact laws, such as those discussed in [51]. However, further research is needed to assess the accuracy of the proposed method under history-dependent contact laws, which will be considered in future developments.

Considering Equations (31) and (32), the normal and tangential contact force vectors are expressed as

$$ {}^{(t)}\mathbf{f}^{\,nor} = {}^{(t)}\overline{f}^{nor\,(t)}\mathbf{C}^{nor} \tag{33} $$

and

$$ {}^{(t)}\mathbf{f}^{\,tan} = {}^{(t)}\overline{f}^{tan\,(t)}\mathbf{C}^{tan} \tag{34} $$

respectively, where the vectors $\mathbf{C}^{nor}$ and $\mathbf{C}^{tan}$ collect the action of the normal and tangential gap functions and are provided in Appendix A. Eventually, the interaction force vector that emerges at the contact surface is expressed as

$$ {}^{(t)}\mathbf{f}^{\,intr} = \sum_{i=1}^{n_s} \left({}^{(t)}\mathbf{f}^{\,nor} + {}^{(t)}\mathbf{f}^{tan} \right) \tag{35} $$

where n_s is the total number of slave nodes that have penetrated the master segment.

The interaction forces at the master and slave discrete field boundaries, introduced in Equation (35), are then projected from the contact surface to the Eulerian grid according to the relation below

$$ {}^{(t)}\mathbf{F}^{cont}_{DI} = \sum_{j=1}^{n_c} N_I^j({}^{(t)}\mathbf{x}_p)\,{}^{(t)}\mathbf{f}^{intr}_j \tag{36} $$

where n_c is the total number of contact grid nodes (see also Figure 6c).

Remark 3. We note that in the present work the boundary material points are not massless. In our view, this results in three interesting algorithm advantages compared to existing methods. First, the contact forces can be naturally projected directly from the slave-master segment pair onto the Eulerian grid at zero computational cost. Also, since the boundary material points have mass, the distribution of the contact forces to the computational nodes is not hindered, that is, there is no requirement for redistributing the contact forces due to zero mass points. Finally, contrary to [24], the normal and tangential contact forces herein are explicitly evaluated from Equations (33) and (34),

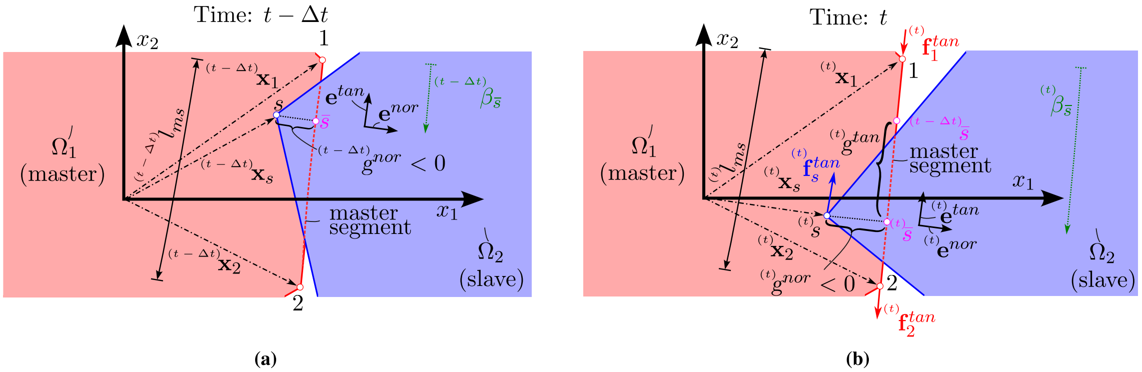

(a) **(b)**

FIGURE 7 | The tangential slip function measures the amount of relative movement of the two contact surfaces, $\partial\Omega_{1\bar{\mathbf{f}}}$ and $\partial\Omega_{2\bar{\mathbf{f}}}$, within a time increment. It is evaluated as per Equation (29). The tangential slip produces the tangential contact forces at the slave boundary material points, $\mathbf{f}_s^{tan}$, and the master segment, $\mathbf{f}_1^{tan}$ and $\mathbf{f}_2^{tan}$.

respectively. Both contact components are projected from the slave-master segment pair to the computational grid. The governing equations are solved without any computational losses.

3.7 | Solution Procedure

In this work, an explicit time integration scheme is utilised to integrate the equations of motion. Considering a forward Euler integration scheme and a momentum formulation of the material point method as detailed in [19], Equation (12) is rewritten as

$$ {}^{(t+\Delta t)}\mathbf{p}_{DI} = {}^{(t)}\mathbf{p}_{DI} + \Delta t\left({}^{(t)}\mathbf{F}^{ext}_{DI} + {}^{(t)}\mathbf{F}^{cont}_{DI} - {}^{(t)}\mathbf{F}^{int}_{DI}\right) \qquad (37) $$

where ${}^{(t+\Delta t)}\mathbf{p}_{DI}$ and ${}^{(t)}\mathbf{p}_{DI}$ are the nodal momentum at time $t + \Delta t$ and t, respectively. The nodal momentum at time t is computed from the material points' mapping as

$$ {}^{(t)}\mathbf{p}_{DI} = {}^{(t)}\mathbf{M}_{DI}\,{}^{(t)}\dot{\mathbf{u}}_{DI} = \sum_{p=1}^{n_p}\left(N_I\left({}^{(t)}\mathbf{x}_{Dp}\right) M_{Dp}\,{}^{(t)}\dot{\mathbf{u}}_{Dp}\right) \qquad (38) $$

The solution procedure of the proposed improved MPM contact algorithm is summarised in Algorithm 1. The first step is to define the initial state for the material points and the computational domain. As indicated in Section 3.6, discrete fields, specifying subsets of material points, are labelled a priori and remain constant to enable tracking of their contact features during the analysis. Additionally, discrete field pairs (e.g., Ω_1-Ω_2 pairs) are established. Prior to analysis, penalty parameters ω^{nor} and ω^{tan}, along with the friction coefficient μ_f, must be defined for each discrete field pair.

As indicated in Section 3.6, discrete fields, specifying subsets of material points, are labelled a priori and remain constant to enable tracking of their contact features during the analysis. Additionally, discrete field pairs (e.g., Ω_1-Ω_2 pairs) are established. Prior to analysis, penalty parameters ω^{nor} and ω^{tan}, along with the friction coefficient μ_f, must be defined for each discrete field pair.

In all numerical tests in this study, a structured computational grid is employed. For instance, a two-dimensional Eulerian grid is defined by the bottom-left coordinates $\mathbf{x}^{min} = \{x_1^{min}, x_2^{min}\}$ and the top-right coordinates $\mathbf{x}^{max} = \{x_1^{max}, x_2^{max}\}$. As emphasised in [43], the use of a structured computational grid facilitates the identification of material points within their parent cells, ensuring robust computational efficiency. The grid spacing, denoted as Δh, is assumed to be uniform across all spatial dimensions. The time step, Δt, for the simulation is chosen following the methodology in Section 4.

After the initialisation step, Equation (37) is numerically solved until the desired simulation time. Time is discretised over n_{steps} time increments. Furthermore, as detailed in Algorithm 1, the basis functions are evaluated prior to grid mapping. Their evaluation process is presented in Algorithm 2 and it is based on the three-step procedure introduced in Section 3.3.1. The equations of motion, Equation (37), are then updated, where the contact forces are computed as outlined in Section 3.6, Equations (35) and (36).

Next, the updated solution needs to be mapped back to material points. In this work, this is implemented utilising a so-called

ALGORITHM 1 | Extended B-Splines-based MPM for frictional contact problems.

```
Data: Define material point properties, computational grid, dynamic parameters (${}^{(0)}\mathbf{x}_{Dp}$, ${}^{(0)}\Omega_{Dp}$, ${}^{(0)}\mathbf{u}_{Dp}$, ${}^{(0)}\dot{\mathbf{u}}_{Dp}$, ${}^{(0)}\ddot{\mathbf{u}}_{Dp}$, ${}^{(0)}\boldsymbol{\varepsilon}_{Dp}$, ${}^{(0)}\boldsymbol{\sigma}_{Dp}$,
      ${}^{(0)}\rho_{Dp}$, $E_{Dp}$, $\nu_{Dp}$, $\mathbf{x}^{min}$, $\mathbf{x}^{max}$, $\Delta h$, $t = 0$, $\Delta t$).
For each discrete field pair define: $\omega^{nor}$, $\omega^{tan}$ and $\mu_f$.
 foreach each time step $m = 0, .., n_{steps} - 1$ do
   $t = t + \Delta t$.
    Reset grid quantities: ${}^{(m)}M_{DI} = 0$, ${}^{(m)}\mathbf{p}_{DI} = \mathbf{0}$, ${}^{(m)}\mathbf{F}^{int}_{DI} = \mathbf{0}$, ${}^{(m)}\mathbf{F}^{ext}_{DI} = \mathbf{0}$ and ${}^{(m)}\mathbf{F}^{cont}_{DI} = \mathbf{0}$, for each grid node $I$.
    Evaluate bases functions (see algorithm 2).
    Map mass, momentum and internal forces from material points to grid nodes: ${}^{(m)}M^{u}_{DI}$, ${}^{(m)}\mathbf{p}_{DI}$, ${}^{(m)}\mathbf{F}^{int}_{DI}$ and ${}^{(m)}\mathbf{F}^{ext}_{DI}$ (see Eq. (13),
    Eq. (38), Eq. (15) and Eq. (16))
    Apply (Dirichlet) boundary conditions: ${}^{(m)}p_{DI,i} = 0$, ${}^{(m)}F^{int}_{DI,i} = 0$, ${}^{(m)}F^{ext}_{DI,i} = 0$ and ${}^{(m)}F^{cont}_{DI,i} = 0$, for each prescribed grid node $I$ in
    direction $i$.
    Update momentum: ${}^{(m+1)}\tilde{\mathbf{p}}_{DI}$ (see Eq. (37))1.
    Map from grid nodes to material points (see algorithm 3).
    Export output (post-processing).
end
```

ALGORITHM 2 | Evaluation of Extended B-Spline basis functions.

```
Calculate grid cells' volume fraction (see Eq. (19).
Classify grid cells into interior, boundary, and exterior ones according to their material point volume fractions as compared to occupation parameter (see Eq. (20)).
Categorise bases functions as either stable, degenerated, or exterior (see step three in Section 3.3.1).
Determine subsets $\mathbb{I}_J$ for degenerated bases functions.
Compute: $\mathbf{N}({}^{(m)}\mathbf{x}_p)$, $\nabla\mathbf{N}({}^{(m)}\mathbf{x}_p)$, for all material points. These correspond to the Original B-Splines as presented in 49, 50.
Compute: $\mathbf{N}^{ebs}({}^{(m)}\mathbf{x}_p)$, $\nabla\mathbf{N}^{ebs}({}^{(m)}\mathbf{x}_p)$, only for degenerated basis functions (see Eq. (25) and Eq. (26)).
```

ALGORITHM 3 | Map from grid nodes to material points. It is based on MUSL algorithm [42, 43].

```
Get nodal velocities and accelerations: ${}^{(m+1)}\tilde{\dot{\mathbf{u}}}_{\mathcal{D}I} = {}^{(m+1)}\tilde{\mathbf{p}}_{\mathcal{D}I} / {}^{(m)}M_{\mathcal{D}I}$ and ${}^{(m+1)}\tilde{\ddot{\mathbf{u}}}_{\mathcal{D}I} = ({}^{(m)}\mathbf{F}^{ext}_{\mathcal{D}I} + {}^{(m)}\mathbf{F}^{cont}_{\mathcal{D}I} - {}^{(m)}\mathbf{F}^{int}_{\mathcal{D}I}) / {}^{(m)}M_{\mathcal{D}I}$. Update material point position: ${}^{(m+1)}\mathbf{x}_{\mathcal{D}p} = {}^{(m)}\mathbf{x}_{\mathcal{D}p} + \Delta t \sum_{I=1}^{n_n} N_I({}^{(m)}\mathbf{x}_{\mathcal{D}p}) \, {}^{(m+1)}\tilde{\dot{\mathbf{u}}}_{\mathcal{D}I}$.
Update material point velocity: ${}^{(m+1)}\dot{\mathbf{u}}_{\mathcal{D}p} = \sum_{I=1}^{n_n} N_I({}^{(m)}\mathbf{x}_{\mathcal{D}p}) \, {}^{(m+1)}\tilde{\dot{\mathbf{u}}}_{\mathcal{D}I}$.
Update material point displacement: ${}^{(m+1)}\mathbf{u}_{\mathcal{D}p} = {}^{(m+1)}\mathbf{x}_{\mathcal{D}p} - {}^{(0)}\mathbf{x}_{\mathcal{D}p}$.
Map momentum from material points to grid nodes: ${}^{(m+1)}\mathbf{p}_{\mathcal{D}I} = \sum_{p=1}^{n_p} N_I({}^{(m)}\mathbf{x}_{\mathcal{D}p}) \left( M_{\mathcal{D}p} \, {}^{(m+1)}\dot{\mathbf{u}}_{\mathcal{D}p} \right)$.
Apply (Dirichlet) boundary conditions: ${}^{(m+1)}p_{\mathcal{D}I,i} = 0$, for each prescribed grid node $I$ in direction $i$.
Get nodal velocities: ${}^{(m+1)}\dot{\mathbf{u}}_{\mathcal{D}I} = {}^{(m+1)}\mathbf{p}_{\mathcal{D}I} / {}^{(m)}M_{\mathcal{D}I}$.
Compute material point gradient velocity: ${}^{(m+1)}\mathbf{L}_{\mathcal{D}p} = \sum_{I=1}^{n_n} \nabla N_I \left( {}^{(m)}\mathbf{x}_{\mathcal{D}p} \right) {}^{(m+1)}\dot{\mathbf{u}}_{\mathcal{D}I}$.
Update gradient deformation tensor: ${}^{(m+1)}\mathbf{F}_{\mathcal{D}p} = \left( \mathbf{I} + {}^{(m+1)}\mathbf{L}_{\mathcal{D}p}\Delta t \right) {}^{(m)}\mathbf{F}_{\mathcal{D}p}$.
Get material point incremental strain: $\boldsymbol{\Delta\varepsilon}_{\mathcal{D}p} = 0.5\Delta t \left( {}^{(m+1)}\mathbf{L}_{\mathcal{D}p} + {}^{(m+1)}\mathbf{L}^T_{\mathcal{D}p} \right)$.
Update material point strains: ${}^{(m+1)}\boldsymbol{\varepsilon}_{\mathcal{D}p} = {}^{(m)}\boldsymbol{\varepsilon}_{\mathcal{D}p} + \boldsymbol{\Delta\varepsilon}_{\mathcal{D}p}$.
Update material point stresses: ${}^{(m+1)}\boldsymbol{\sigma}_{\mathcal{D}p} = \partial \, {}^{(m+1)}\psi_{el\mathcal{D}p} / \partial \, {}^{(m+1)}\boldsymbol{\varepsilon}_{\mathcal{D}p}$.
```

MUSL approach [42, 43] to avoid numerical instabilities associated with potentially small grid nodal masses. It should be noted that the boundary material points are treated in the same manner as the material points in the bulk, for example, position, strain, stress update, and so forth. The procedure is presented in Algorithm 3.

Remark 4. The proposed algorithm detects contact only when a boundary material point from the slave boundary solid body interpenetrates a master segment formed by boundary material points from the master solid body. In this case, contact forces are generated to prevent further interpenetration of the two bodies until equilibrium is achieved in subsequent time steps. It is important to note that the negligible interpenetration observed at equilibrium is a direct result of the penalty method employed. This method weakly enforces the contact constraints (see also Figure 2), allowing for small interpenetration, which is typical of penalty-based approaches. This controlled overlap does not affect the accuracy or stability of the simulation, as demonstrated in the numerical examples in Section 4. The chosen penalty parameters (determined by Equation (40)) and time step (constrained by the Courant–Friedrichs–Lewy condition, Equation (39)) ensure that this small interpenetration does not compromise the overall physical correctness of the results.

Remark 5. In this work, material points update uses a Particle-In-Cell (PIC) approach. To this point, two main methods are used to update the velocity and position of material points in the literature, that is, PIC and Fluid Implicit Particle (FLIP) (see, e.g., [52]). A PIC update filters velocity in each time step, which causes unwanted numerical diffusion, while FLIP eliminates that diffusion but may retain too much noise. Noise reduction via null space removal techniques attempts to minimise these errors [21, 52]. In [53] the affine PIC method has been introduced to reduce diffusion and improve conservation. Nevertheless, energy conservation and updating the velocity and position of material points remain open research issues. Very recently, [54], have proposed a novel time-stepping approach based on an efficient approximation of the CFL condition to enhance momenta and energy conservation in the MPM. We point out, however, that such instabilities are different from the ones examined in this work and that pertain to the algorithmic treatment of frictional contact. However, revisiting the proposed formulation and further extending it using the aforementioned approaches is an interesting research direction that we would like to consider as future work.

4 | Numerical Examples

This section presents numerical verification of the proposed model, focusing on one- and two-dimensional contact problems. Results are compared with literature and analytical solutions, including tests with OBS, CPDI2, and state-of-the-art MPM contact implementations. A comparison between EBS and OBS is important in contact problems to illustrate the influence of numerical integration errors at the boundary grid cells and ultimately at the evolved contact forces. In addition, both EBS and CPDI approximations [37] have been implemented and compared using the proposed penalty contact algorithm. The CPDI implementation of the contact algorithm employs the domain edges of material points, which are located at the boundary of each solid body (master, slave), to represent the boundary and facilitate the tracking of contact features throughout the analysis. These boundary edges are treated as massless.

Quadratic B-Splines (C^1)are employed for the background grid. In all two-dimensional problems, plane strain conditions are assumed. In addition, linear elastic material response is considered for all benchmarks except from Section 4.4 where a hyperelastic compressible Neo-Hookean material law has been utilised.

The explicit time integration scheme's stability is maintained by limiting the time increment, Δt, with the upper bound:

$$\Delta t \leq 0.1\Delta t_{cr} \tag{39}$$

Here, $\Delta t_{cr} = \Delta h / c_0$ is the critical time step defined by the Courant–Friedrichs–Lewy (CFL) condition, where $c_0 = \sqrt{E/\rho}$ represents the speed of sound in solids. Although a higher factor of 0.1 could be used, a smaller factor has been chosen to ensure greater accuracy and stability in the numerical examples. It has been observed that accuracy and stability are maintained with factors up to 0.4 in the examples presented in this work.

To prevent contact violation, penalty parameters ω^{nor} and ω^{tan} need substantial values, yet excessively large ones can induce numerical instabilities. Thus, the following relation is employed to determine these parameters:

$$\omega^{nor} = \omega^{tan} = \frac{1}{\Delta h / E} \tag{40}$$

This equation, used in previous works [28, 55, 56], demonstrates stability in the conducted numerical tests, avoiding associated instabilities. The proposed method has been developed using an in-house FORTRAN code.

4.1 | One-Dimensional Compression of Two Contacting Bars Under Self Weight

This example investigates the one-dimensional compression of two bars under self-weight, as illustrated in Figure 8. This serves to validate the proposed algorithm against analytical solutions and highlight its advantages over OBS and CPDI2 variants.

The setup involves two bars, each of length 0.3 m, positioned one on top of the other (see Figure 8). The bottom bar is fixed at its lower edge with $u(x = 0) = 0$. To impose this fixed boundary condition, a “rigid” spring with a stiffness of $65 \cdot 10^9$ N/m is added to the boundary material point. This ensures fixed boundary conditions even when the control point of the Eulerian grid does not coincide with the boundary material point. The spring stiffness was chosen empirically by incrementally increasing it until convergence in the results was achieved. Excessively large values can cause numerical instabilities in the explicit time integration scheme and necessitate an exceptionally small time step to satisfy the CFL condition. Both bars share identical material properties: mass density $\rho = 2,783$ kg/m^3, Young’s modulus $E = 50.5$ GPa, and cross-sectional area $A = 1$ m^2.

In this example, a one-dimensional Eulerian grid is defined with a grid spacing of $\Delta h = 0.1$ m. Each discrete field has initially a grid cell density of 4 material points per cell, along with 2 boundary material points. The time step, Δt, follows Equation (39), set as $\Delta t = 0.1\Delta t_{cr} = 2.34753 \cdot 10^{-6}$ s. The bars are initially stress-free at $t = 0$, and a quasi-static response is ensured by gradually increasing the gravity force to $g = -9.81$ m/s^2 over 0.0281 s (equivalent to 12,000 time steps), 200 times the elastic wave transit time in the bars, that is, $(1/c_0) \cdot l_0 \cdot 200$. The EBS adopts an occupation parameter of 0.75. The normal penalty parameter, calculated using Equation (40), is set to $\omega^{nor} = 505 \cdot 10^9$ N/m^3.

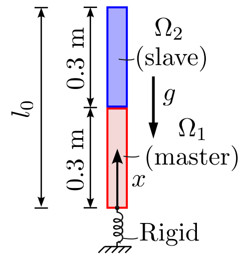

FIGURE 8 | One-dimensional compression of two contacting bars under self-weight. Geometry and boundary conditions.

To examine the influence of the Eulerian grid on the evaluated stress as a result of incomplete integration, 6 cases are considered as initial bar locations (termed as bar offsets herein), that is, 0, +0.016, +0.033, +0.05, +0.066, and +0.083 m. The master bar is initially located at position 0.2 m on the Eulerian grid, and it is offset as per the bar offset cases.

The analytical solution for the Cauchy stress over the bars’ length, σ, is computed from the Equation (41) [57].

$$\sigma(x) = \sigma(0)\frac{(1 - x/l_0) + \alpha(x/l_0)}{1 - \alpha(1 - \alpha)(x/l_0)} \tag{41}$$

where $\sigma(0) = \rho g A l_0$ and $\alpha = \sigma(0)/(2E)$. Total weight of the bar is $W = -16,380.738$ N.

The stress computations, illustrated in Figure 9 for OBS, CPDI, and EBS against the analytical solution, highlight the accuracy of EBS in predicting stress across two bar offsets, that is, +0.00 and +0.05 m. Regardless of the bar’s position relative to the Eulerian grid, EBS and CPDI provide precise stress predictions. In comparison, OBS fails to converge accurately and exhibits substantial errors at the contact point. Stress noise and numerical integration errors are evident with OBS, especially at the master bar’s bottom edge for bar offset +0.050, see Figure 9b.

The dimensionless error, calculated using Equation (42), further emphasises these differences.

$$\text{Error} = \sum_{p=1}^{n_p} \frac{\left|\sigma_p^{\text{numerical}} - \sigma_p^{\text{analytical}}\right| \Omega_p}{|W| l_0} \tag{42}$$

As illustrated in Figure 10, the OBS error increases due to incomplete numerical integration, whereas the errors for EBS and CPDI remain consistently low. Moreover, the results for EBS demonstrate a lower error compared to those obtained with CPDI.

Furthermore, Figure 11a,b display the computed stresses at critical points along the bars for different offsets. Figure 11a demonstrates that both EBS and CPDI maintain relatively stable values compared to the analytical solution, with EBS showing a generally lower error. Furthermore, Figure 11b illustrates contact stresses, where CPDI not only deviates significantly from the analytical solution but also exhibits substantial differences between master top and slave bottom stresses. In contrast, EBS contact stresses show differences of up to 3%.

To further investigate how the mass distribution in the boundary material points affects stress estimates, Figure 12 (bar offset +0.00) and Figure 12 (bar offset +0.05) display results for three different mass percentages relative to the total mass of the domain: 0.1%, 1%, and 5%. The stress estimates show significant deviations from the analytical solution when the mass percentage exceeds 1%. In comparison, a mass percentage of 0.1% yields results that are closer to the analytical solution, thereby justifying the choice of this percentage for the current work.

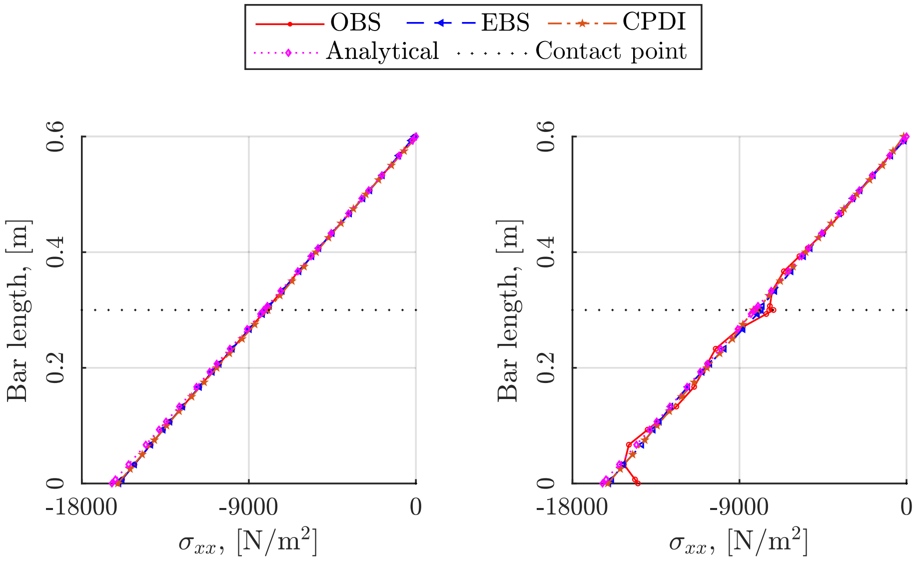

(a) Bar Offset: 0.00 m **(b)** Bar Offset: 0.05 m

FIGURE 9 | One-dimensional compression of two contacting bars under self-weight. Stress over bar length for two bar offsets, that is, +0.00 and +0.05 m. The proposed frictional contact EBS-based algorithm (blue dashed line) provides good estimates of the bars' stress along their length, regardless of the position of the bar with respect to the Eulerian grid. Similarly, the CPDI-based variant of the algorithm yields good stress estimates too (brown line). In comparison, OBS (red line) fails to converge to the accurate stress, showing severe errors at the location of the contact and bottom points.

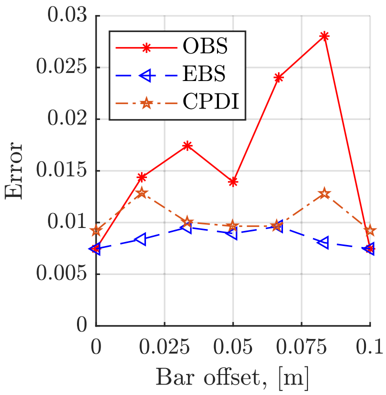

FIGURE 10 | One-dimensional compression of two contacting bars under self-weight. Stress error for various bar offsets within the Eulerian grid. The stress error is retained at low levels with the proposed EBS (blue line) and CPDI variant (brown line). This is not the case for OBS, whose stress error increases with the bar offset due to incomplete numerical integration (red line). Additionally, the results for EBS show a smaller error relative to those achieved with CPDI.

4.2 | Longitudinal Impact of Two Bars

The second example concerns the investigation of the longitudinal impact of two one-dimensional bars, characterised by different initial velocities, thereby resulting in a collision. The aim of this example is to ascertain the post-impact velocities of the objects, as well as the corresponding impact force over time. In the present scenario, a one-dimensional case is examined where a bar with a length of $l_1 = 0.2$ m collides with another bar with a length $l_2 = 0.4$ m as depicted in Figure 13.

Both bars possess identical material properties, with Young's modulus $E = 50.5$ GPa, cross section $A = 1\ \mathrm{m}^2$, and mass density $\rho = 2,783\ \mathrm{kg/m}^3$. All the points on the left bar have the same initial velocity, that is, $\dot{u}_1 = v_0 = 1$ m/s, while the bar on the right is stationary $\dot{u}_2 = 0$ m/s. The two bars are unstressed at $t = 0$. The solution of this problem can be derived from the one-dimensional wave equation as shown in Figure 13. The simulation is performed with a grid spacing $\Delta h = 0.390625$ mm. The cell density is 4 material points per grid cell, while extra material points are added at the bar's edges to track their boundary. A total of 6148 material points was used. The time step is chosen to be $\Delta t = 0.00917$ µs and satisfies the CFL condition. The value of the normal penalty parameter is $\omega^{nor} = 1,29,280\ \mathrm{N/mm}^3$. To alleviate any stress "noise" during the impact of the two bars, the proposed EBS-based MPM is utilised with the occupation parameter $C_c = 0.75$. Simulation is also performed with OBS to highlight the merits of the proposed method. The one-dimensional Eulerian grid is formed with $x^{min} = 0$, $x^{max} = 1$ m. The results from the simulation are shown in Figures 14 and 15 for the bars' velocity and stress over 5 time instances, $t \in [l_1/c_0, 2l_1/c_0, 3l_1/c_0, 4l_1/c_0, 5l_1/c_0] = [46.95, 93.9, 140.85, 187.8, 234.75]$ µs.

The two objects undergo contact until $t = 4l_1/c_0$, which is the point in time at which the reflected wave in the second object reaches the point of contact. Given the stress-free nature of the first object, the wave reflects back instead of entering the first object in accordance with the stress-free boundary condition. This is illustrated in Figures 14c and 15c where both the mean value of the velocity of the stress are zero. Following this, the objects lose contact. The final velocity of the first object is $\dot{u}_1 = 0$, whereas that of the second object is $\dot{u}_2 = v_0/2$. This is shown in Figure 14d. Notably, as depicted in Figure 14e, the second object continues to undergo oscillations as a result of the travelling stress wave, while the first object remains stationary. Velocity and stress numerical solutions also result in good agreement with the analytical solutions provided in [46].

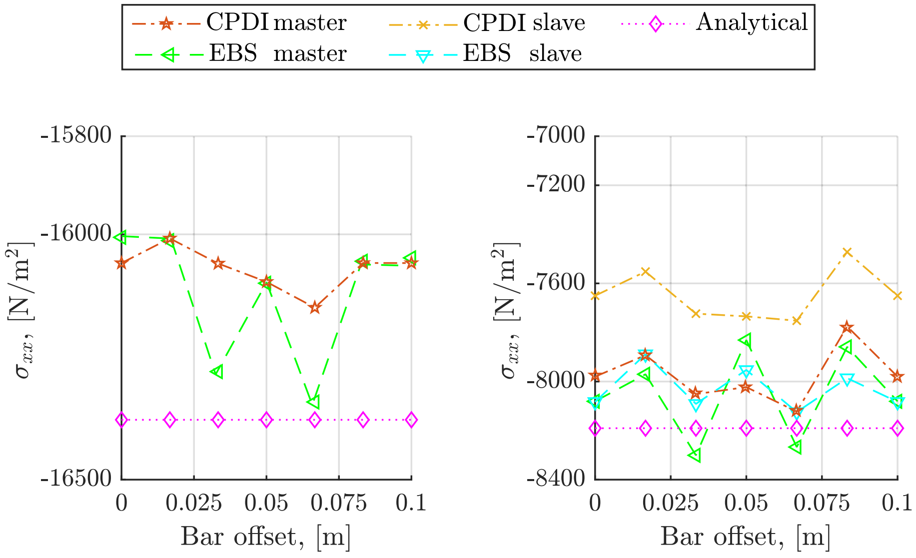

(a) **(b)**

FIGURE 11 | One-dimensional compression of two contacting bars under self-weight. (a) Master bar bottom stress, and (b) master bar top, slave bar bottom master bar top stress, slave bar bottom. It is illustrated that both EBS and CPDI exhibit relatively stable values in comparison to the analytical solution, with EBS generally demonstrating a lower error. Additionally, Figure 11b shows that CPDI deviates considerably from the analytical solution and shows significant discrepancies between the master top and slave bottom stresses. In contrast, the contact stresses obtained using EBS display differences of up to 3%.

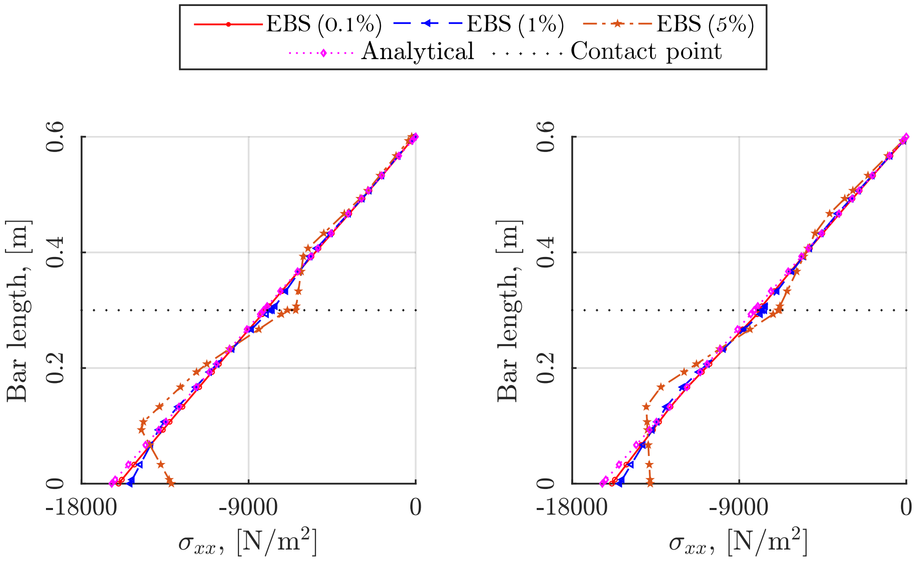

(a) Bar Offset: 0.00 m **(b)** Bar Offset: 0.05 m

FIGURE 12 | One-dimensional compression of two contacting bars under self weight. Stress estimates for mass percentages of 0.1%, 1%, and 5%. Results deviate significantly from the analytical solution for percentages greater than 1%, while 0.1% provides closer agreement, justifying its use in this work.

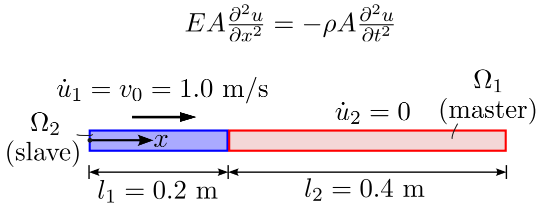

FIGURE 13 | Longitudinal impact of two bars. Geometry and initial conditions.

As a further investigation within this example, a parametric study is performed for the grid spacing of the Eulerian grid as shown in Figure 16. Two additional coarser grid spacings, namely 12.5 and 6.25 mm, are examined, with EBS results compared against those obtained using CPDI. The time step is then chosen as 0.2934 and 0.1467 μs, respectively. Similarly, the number of materials points used are 196 and 388, respectively. The value of the normal penalty parameter is also adjusted at 4040 and 8080 N/mm^3. Figure 16 presents the bars' stress over their length for two time

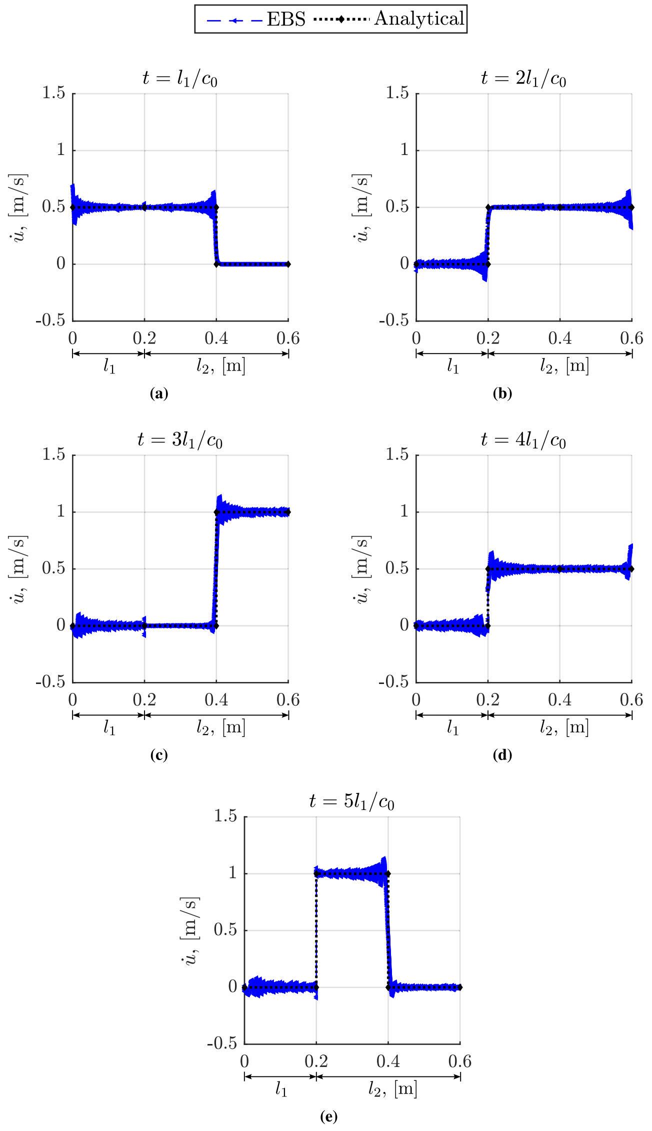

(a) (b) (c) (d) (e)

FIGURE 14 | Longitudinal impact of two bars. Velocity over bars' length for time instances, (a) $l_1/c_0 = 46.95$ µs, (b) $2l_1/c_0 = 93.9$ µs, (c) $3l_1/c_0 = 140.85$ µs, (d) $4l_1/c_0 = 187.8$ µs, and (e) $5l_1/c_0 = 187.8$ µs. The proposed penalty EBS contact algorithm is utilised for the numerical simulations. The analytical solutions are also plotted with a black dotted line. EBS provides good accuracy compared to the analytical solutions.

instances, that is, $t = 2l_1/c_0$ and $t = 4l_1/c_0$. In this, it is shown that EBS yields better accuracy over CPDI and converges to the analytical solutions faster.

The energy conservation is also examined in this example. The kinetic, stored, and total energy for each time step for all material points are evaluated as

$$\mathcal{K} = \sum_{p=1}^{n_p} \left(\frac{1}{2} (\dot{u}_{p_x}^2 + \dot{u}_{p_y}^2) M_p \right), \ \mathcal{W} = \sum_{p=1}^{n_p} \left(\psi_p \Omega_p \right), \ \mathcal{T} = \mathcal{K} + \mathcal{W} \quad (43)$$

respectively.

Figure 17a–d present the kinetic, stored, and total energies for two grid spacings, that is, $\Delta h = 12.5$ and $\Delta h = 6.25$ mm, respectively. Numerical results for both EBS and CPDI are presented. The findings indicate that EBS demonstrates better energy conservation compared to CPDI. Although CPDI's energy conservation improves with finer grid spacing, EBS achieves energy convergence even with relatively coarse computational grids.

4.3 | Hertz'S Contact Benchmark Problems

These examples illustrate the proposed method's ability to evaluate contact areas using Hertz contact analyses.

4.3.1 | Scenario 1: Hertz Contact Between Two Discs

In the first Hertz contact problem, we examine two contacting discs as depicted in Figure 18. Both discs have a radius of $R = 1$ cm, a Young's modulus of $9.453 \cdot 10^{10}$ Pa, and a Poisson's ratio of 0.07. The discs experience body forces F that compel them to approach each other. This benchmark has previously been investigated by [24] using a hybrid penalty and grid-based contact method for MPM. Their results provide a basis for comparison with our proposed approach. In particular [24], determined the force-contact length relationship for applied force F across three grid spacings, Δh: $R/10$, $R/20$, and $R/40$. They explored two orientations of the line through the disc centres relative to the x-axis: (i) 0° and (ii) 45°.

We conduct comparable simulations to those in [24]. The bars are stress-free at $t = 0$, and a quasi-static response is achieved by incrementally raising body forces F over 400 µs. For consistency with [24], we use 100 master segments for the boundary of each disc in the 0° configuration and 200 segments for the 45° configuration. The simulated contact length is determined by aggregating penetrated master segments.

Simulation results for the 0° and 45° configurations are displayed in Figure 19a,b, respectively. Analytical expressions of the force-contact length relationship, detailed in [24, 58], are also included in the figures for comparison with the numerical simulations. The analytical relationship between the contact force F and the contact region (semi-contact-width) a is

$$\alpha = \sqrt{\frac{4FR^*}{\pi E^* L}} \quad (44)$$

where $\frac{1}{R^*} = \frac{1}{R_1} + \frac{1}{R_2}$ and $\frac{1}{E^*} = \frac{1-\nu_1^2}{E_1} + \frac{1-\nu_2^2}{E_2}$ are the effective radius and elastic modulus, respectively, and L is the length of the cylinder, assumed to be 1 m.

All simulations using the proposed method align well with expected and computed results from [24]. As noted in [24] and depicted in Figure 19a, deviations from expected results are more noticeable in the final loading step. The responses of cases $R/10$ and $R/20$ are similar, while the $R/40$ prediction underestimates the contact area, albeit suggesting more accurate estimates than those reported in [24].

In Figure 19b, excellent agreement with the expected result is also observed for the 45-degrees case. Notably, the simulation

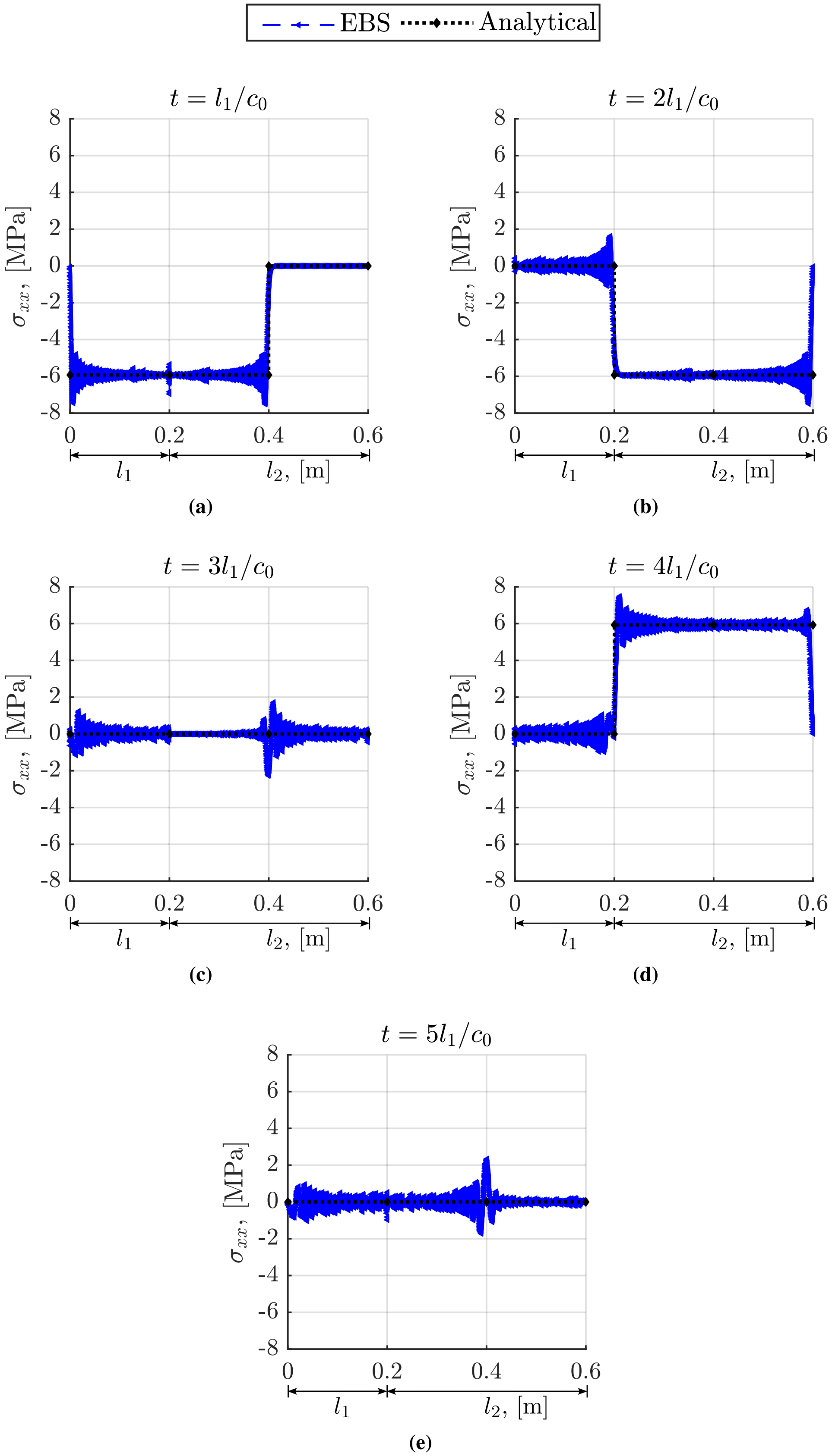

FIGURE 15 | Longitudinal impact of two bars. Stress over bars' length for time instances, (a) $l_1/c_0 = 46.95$ µs, (b) $2l_1/c_0 = 93.9$ µs, (c) $3l_1/c_0 = 140.85$ µs, (d) $4l_1/c_0 = 187.8$ µs, and (e) $5l_1/c_0 = 187.8$ µs. The proposed penalty EBS contact algorithm is utilised for the numerical simulations. The analytical solutions are also plotted with a black dotted line. EBS provides good accuracy compared to the analytical solutions.

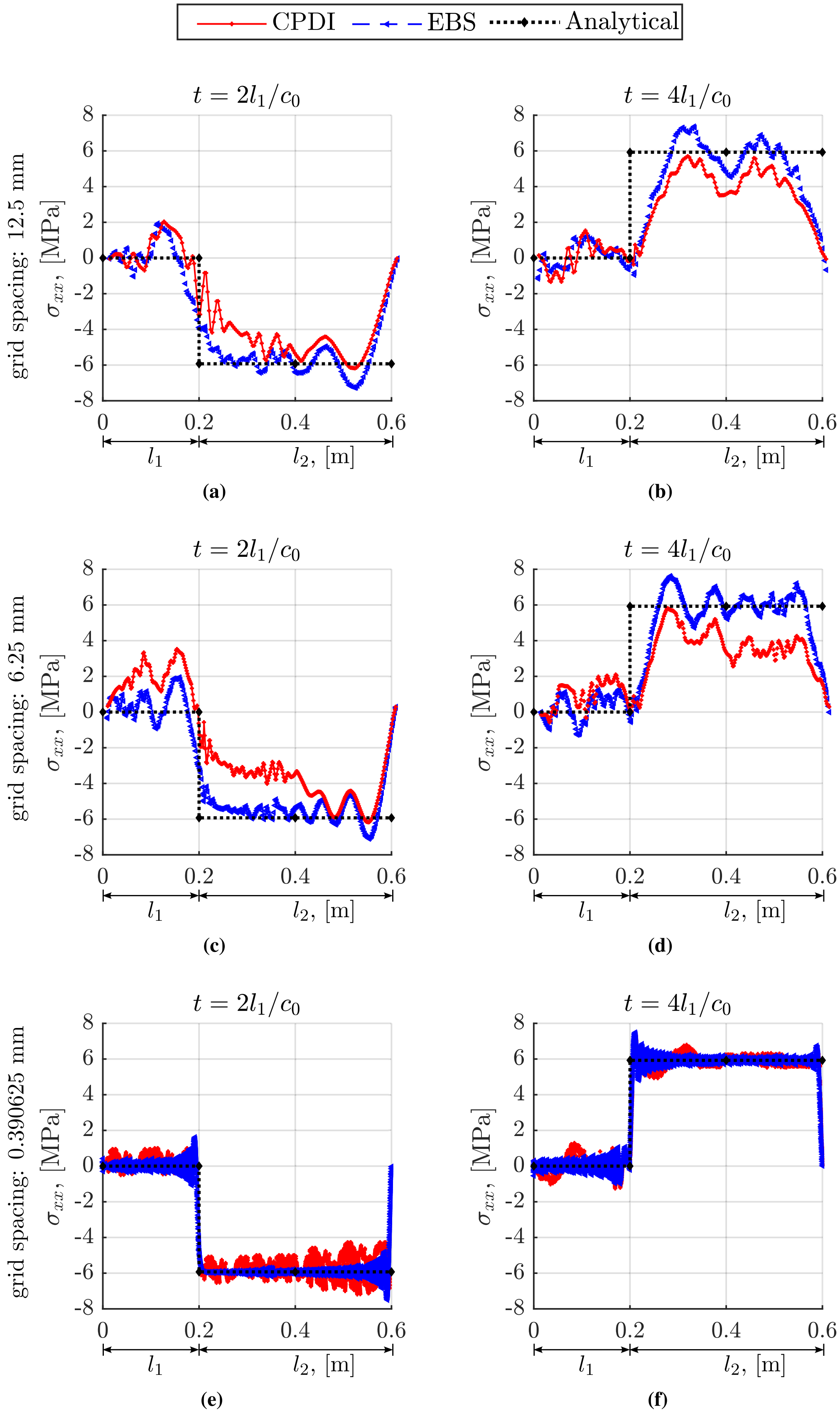

FIGURE 16 | Longitudinal impact of two bars. Stress over bars' length for time instances, $t \in [2l_1/c_0, 4l_1/c_0] = [93.9, 187.8]$ μs, and three grid spacings, $\Delta h \in [12.5, 6.25, 0.390625]$ mm. Two numerical simulations are considered with CPDI (red line) and EBS (blue line). The analytical solutions are also plotted with a black dotted line. EBS yields better accuracy over CPDI and converges to the analytical solutions faster.

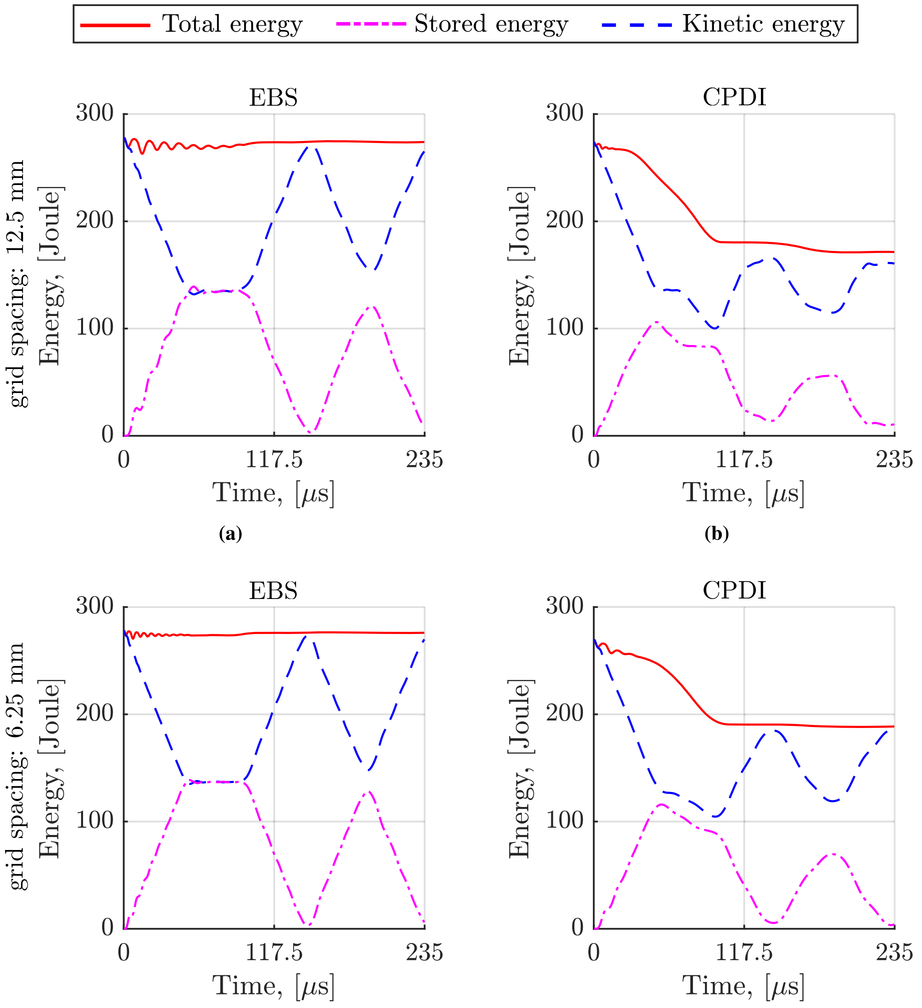

(a) (b) (c) (d)

FIGURE 17 | Longitudinal impact of two bars. Kinetic, stored, and total energies for both EBS and CPDI are presented, and for grid spacings of $\Delta h = 12.5$ and $\Delta h = 6.25$ mm. The results indicate that EBS demonstrates better energy conservation compared to CPDI. While CPDI's energy conservation improves with grid spacing refinement, EBS achieves convergence in energy even with relatively coarse computational grids.

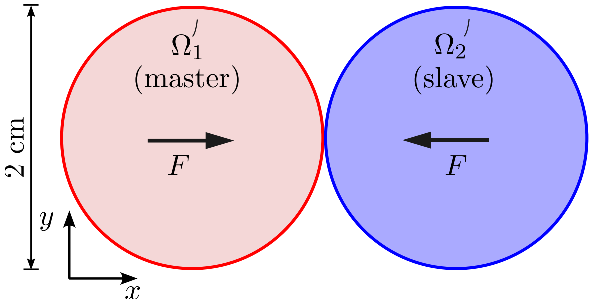

FIGURE 18 | Hertz contact between two disks. Scenario 1. Geometry and boundary conditions.

estimates show better alignment with the expected result when the grid spacing resolution is finer, specifically with $R/40$. The increased resolution of the domain boundary, achieved with 200 master segments, further improves prediction accuracy, as also highlighted in [24]. Importantly, the results obtained with the current method suggest better agreement with the expected outcome compared to those reported in [24]. A visual representation of the results obtained with the proposed penalty EBS is shown in Figure 20 for the first and last loading steps.

4.3.2 | Scenario 2: Hertz Contact Between a Demi-Sphere and a Rigid Plane

Scenario 2 explores Hertz's contact benchmark, involving a demi-sphere and a rigid plane. This aims to validate the proposed MPM implementation for non-flat contact surfaces by comparing the analytical solution of the pressure distribution and the contact area size. Previous studies [22] are referenced for discussion. The problem's configuration and boundary conditions are illustrated in Figure 21.

For the slave body, Young's modulus is $E_2 = 10$ GPa, and Poisson's ratio is $\nu_2 = 0$. The master body is rigid. Three Eulerian grid spacings are considered: $\Delta h = 0.2$, $\Delta h = 0.1$, and $\Delta h = 0.05$ mm. The simulation duration is 175 µs. An occupation parameter of 0.50 is chosen for EBS generation, and the friction coefficient is $\mu_f = 0$. The two bodies are unstressed at $t = 0$. An external load of $F = 156.7$ N is gradually applied throughout the simulation to mimic conditions approaching a steady state.

The analytical solution of the contact pressure distribution along the contact surface is evaluated from the relation below

$$\sigma_{yy} = -\sigma_{yy}^{max}\sqrt{1-\left(\frac{s}{b}\right)^2}, \text{ for } 0 \leq s \leq b \tag{45}$$

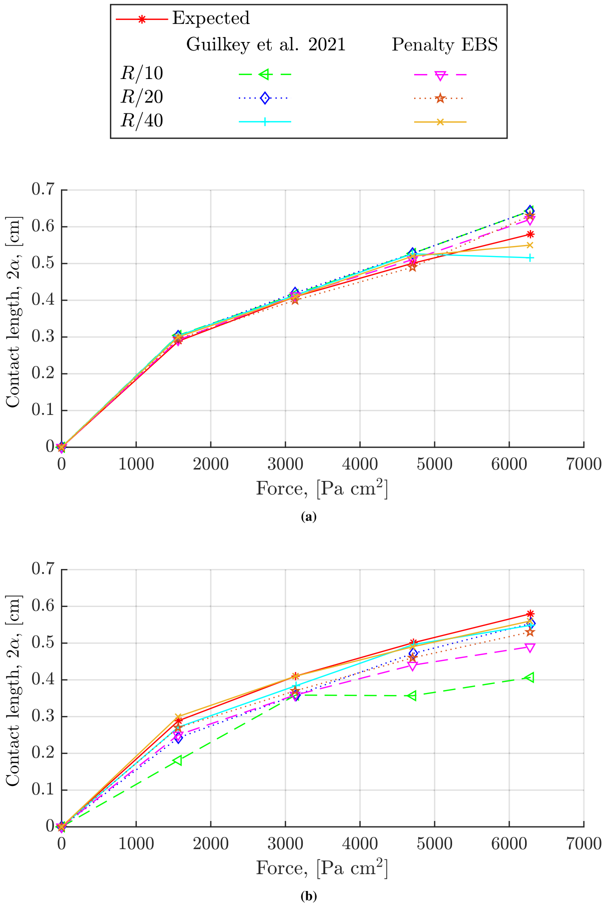

FIGURE 19 | Hertz contact between two discs. Scenario 1. Contact length analysis for two discs pushed together by body force. Numerical results at three grid resolutions are compared to Hertz contact analysis results and the simulations in [24]. (a) 0° and 100 master segments, and (b) 45° and 200 master segments.

where $\sigma_{yy}^{max} = \frac{2F}{\pi b}$ and $b = 2\sqrt{\frac{(2FR)}{\pi E'}}$. The effective Young's modulus is defined as $E' = \frac{2}{E'} = \frac{1-\nu_1^2}{E_1} + \frac{1-\nu_2^2}{E_2}$ while $R = \frac{R_1 R_2}{R_1+R_2}$ is the equivalent body radius, where R_1, R_2 are the radii of the two contact surfaces, respectively. The radius of the master body is infinite.

The σ_{yy} results from the EBS-based MPM are depicted in Figure 22 for the three grid spacings. The results suggest a convergence of contact pressure to the analytical solution with increasing mesh refinement, consistent with [22]. In addition, stress estimates are investigated using the recently proposed logistic regression approach, as described in [21]. The results, displayed in Figure 22b, d, and f for three grid spacings, indicate that logistic regression underestimates stress estimates in the contact region. These findings are consistent with the observations noted in [24], suggesting that this method may encounter difficulties in scenarios involving small deformations between stiff objects, as exemplified by this numerical case.

To further assess the proposed approach's accuracy, Figure 23 illustrates the normalised relative Root Mean Square Error

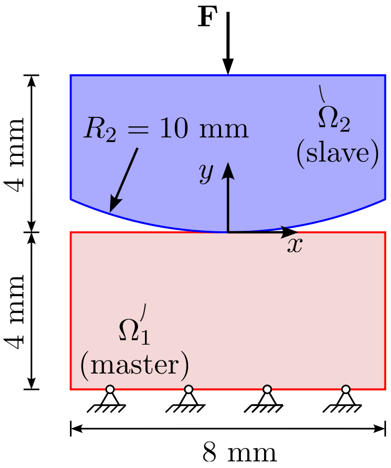

FIGURE 21 | Hertz contact between a demi-sphere and a rigid plane. Scenario 2. Geometry and boundary conditions.

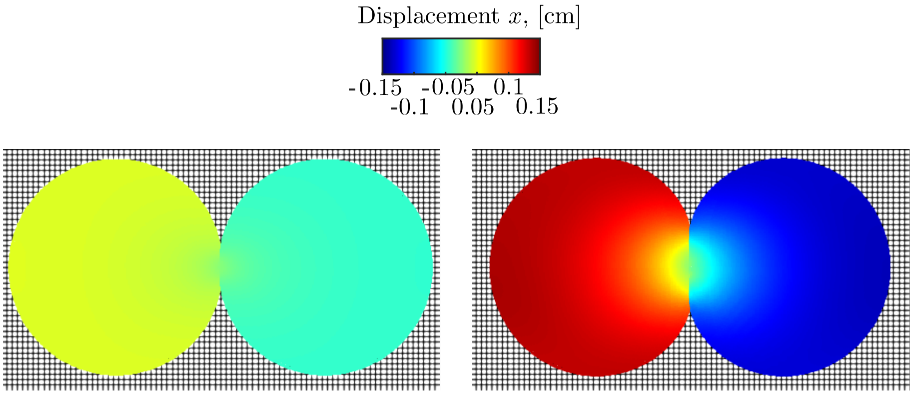

(a)

(b)

FIGURE 20 | Hertz contact between two discs. Scenario 1. Contact length analysis for two discs pushed together by body force. Penalty EBS results. Displacement x for grid spacing $R/20$, 0°, and 100 master segments for the domain boundary. (a) First loading step, and (b) last loading step. These loading steps correspond to the markers shown in Figure 19a.

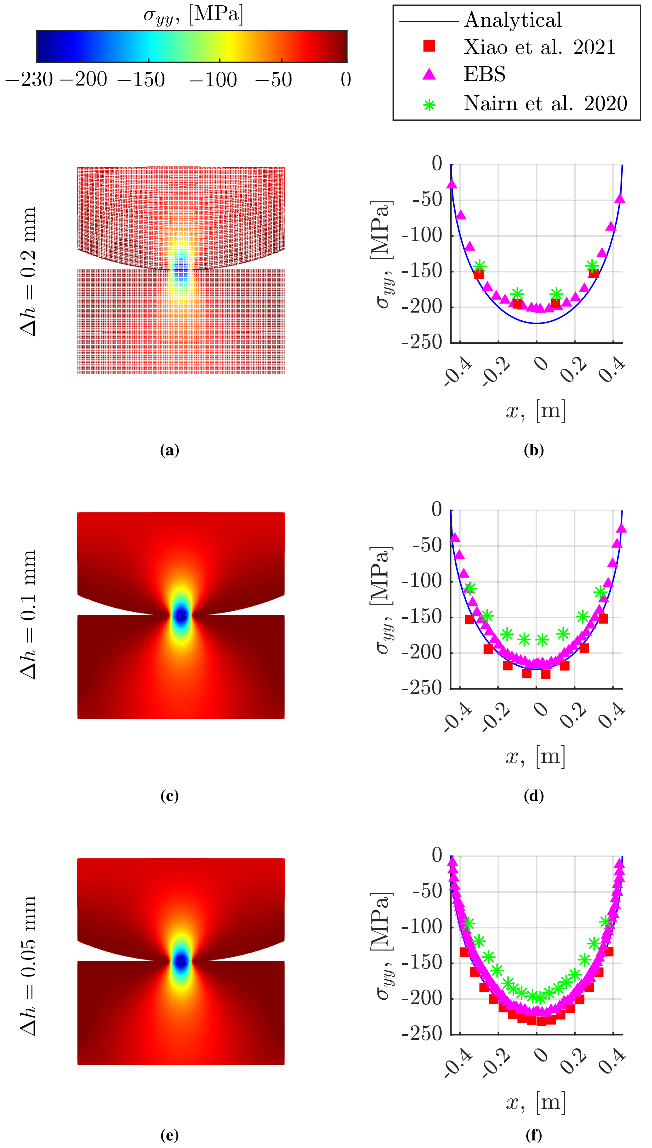

FIGURE 22 | Hertz contact between a demi-sphere and a rigid plane. Scenario 2. Results of σ_{yy} with the proposed EBS-based MPM and three grid spacings, that is, (a) and (b) $\Delta h = 0.2$ mm, (c) and (d) $\Delta h = 0.1$ mm, and (e) and (f) $\Delta h = 0.05$ mm. The simulation results imply that, as the mesh undergoes iterative refinement, the contact pressure progressively nears and aligns with the analytical solution. This is also reported in the findings of [22], which are marked in the graphs. Moreover, stress estimates are investigated using the logistic regression approach from [21]. The results indicate that logistic regression underestimates stress in the contact region, consistent with the observations in [24], suggesting challenges in scenarios with small deformations between stiff objects.

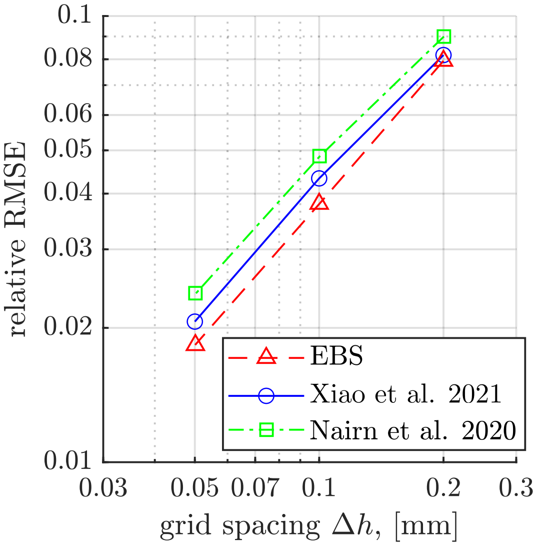

FIGURE 23 | Hertz contact between a demi-sphere and a rigid plane. Scenario 2. Convergence of the relative root mean square error (RMSE) (see Equation (46)) for simulated contact pressures using various grid spacings and EBS-based MPM. Computed error is comparable with the results reported in [22]. The RMSE also indicates that the EBS yields better accuracy compared to both [22] and [21] MPM contact variants.

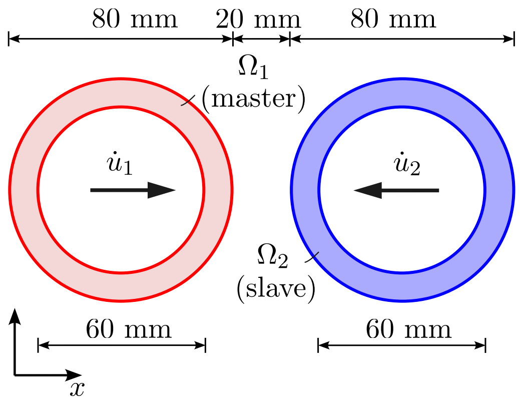

FIGURE 24 | Impact of two compressible Neo-Hookean cylinders. Geometry and boundary conditions.

(RMSE) for pressure values across contact surface material points. The relative RMSE is formulated as

$$\text{relative RMSE} = \frac{\sqrt{\frac{\sum_{p=1}^{\mathcal{N}_p}\left(\sigma_{yy}^{\text{numerical}}-\sigma_{yy}^{\text{analytical}}\right)^2}{\mathcal{N}_p}}}{\sigma_{yy}^{max}} \tag{46}$$

where $\mathcal{N}_p$ is the total number of material points at the contact surface $\partial\Omega_2$. As anticipated, the relative RMSE diminishes as the refinement of the Eulerian grid takes place. The RMSE also indicates that the EBS yields better accuracy in comparison to both [22] and [21] MPM contact variants.

4.4 | Impact of Two Compressible Neo-Hookean Cylinders

This example examines the collision of two hollow elastic cylinders as shown in Figure 24. This benchmark has been extensively investigated in the literature, see, for example, [27], where discrete velocity fields [17] have been employed and most recently by [23] using a TLMPM formulation. The aim of this example is to demonstrate that the proposed method results in no early contact errors. Both cylinders are considered purely elastic, and hence energy conservation is also examined.

The material is a compressible Neo-Hookean which the stored energy density is defined as [47]

$$\psi = \frac{\mu}{2}\left(I_c - d\right) - \mu \ln J + \frac{\lambda}{2}(\ln J)^2 \tag{47}$$

where $I_c = \mathrm{Tr}(\mathbf{C})$ is the first principal invariant of the right Cauchy–Green strain tensor $\mathbf{C} = \mathbf{F}^T\mathbf{F}$ and $J = \det(\mathbf{F})$. The symbol Tr denotes the trace of the tensor $\mathbf{C}$ while $d = 2$ corresponds to the dimension of the problem. The material properties are expressed with the Lamé constants, that is, $\mu = 26.1$ and $\lambda = 104.4$ MPa. The Cauchy stress tensor derives from Equation (47) and is expressed as

$$\sigma = \frac{1}{J}\left(\mu(\mathbf{F}\mathbf{F}^T - \mathbf{I}) + \lambda \ln(J\mathbf{I})\right) \tag{48}$$

where $\mathbf{I}$ is the second-order identity tensor.

The mass density is $\rho = 1{,}010$ kg/m^3 and the grid cell size is considered to be $\Delta h = 1.25$ mm. The magnitude of the cylinders' initial velocity is 0.03 mm/μs. Frictional contact is not employed in this configuration, that is, $\mu_f = 0$. Both solid bodies are unstressed at $t = 0$.

The evolution of deformation over time is depicted across various time steps in Figure 25, employing the proposed penalty EBS method. Figure 26 also contrasts the proposed method with the no-penalty EBS, penalty CPDI and TLMPM formulation as outlined in [23]. The no-penalty EBS results were obtained by considering a common discrete field for both solid bodies. In Figure 26, it becomes apparent that when a penalty method is not used the MPM implementation leads to early contact errors as the two solid bodies make contact. In comparison, the proposed penalty EBS, the penalty CPDI and the TLMPM variants have successfully eliminated such errors. However, as illustrated in Figure 27, the results obtained with the proposed method demonstrate better energy conservation compared to TLMPM. The TLMPM results depicted in Figures 26d and 27c are obtained using hat weighting functions, which, as suggested in [23], contribute to enhanced energy conservation. Finally, upon comparing the energy conservation results from the EBS and CPDI methods, as shown in Figure 27a, b, respectively, it is evident that the two methods demonstrate a high degree of agreement. Consequently, the Mean Squared Error (MSE) is calculated

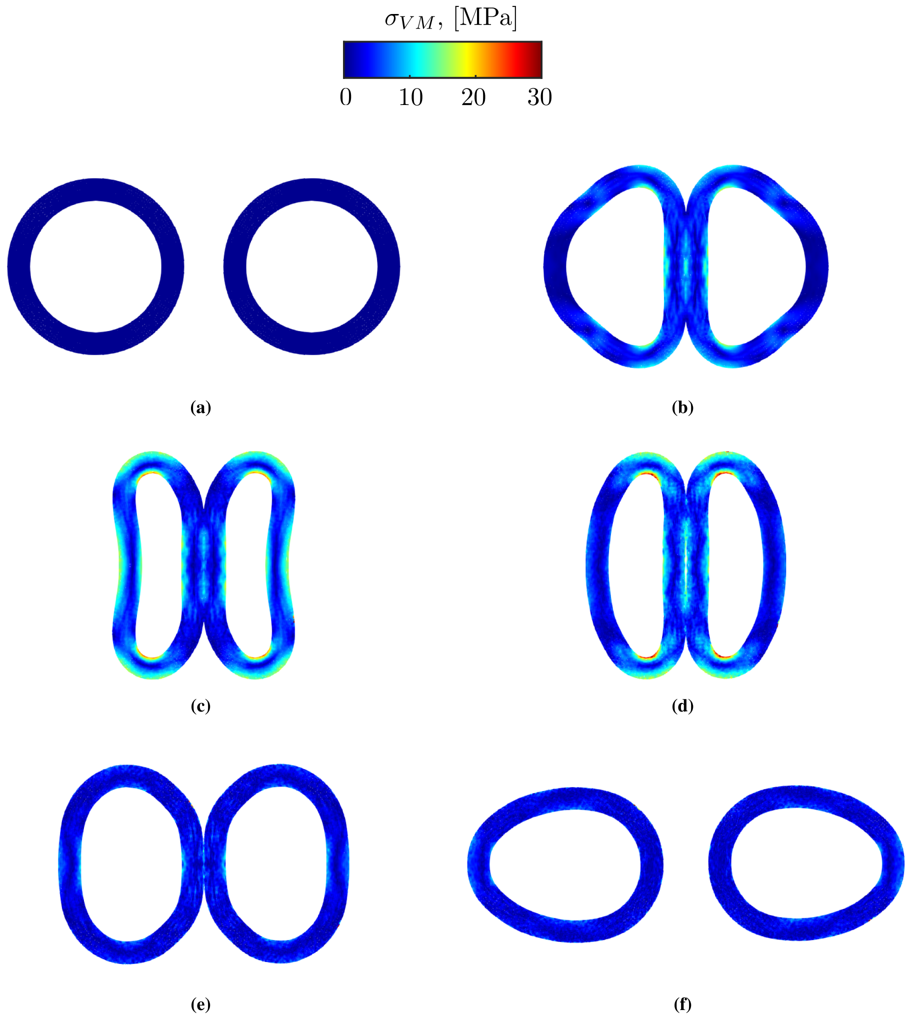

(a) (b) (c) (d) (e) (f)

FIGURE 25 | Impact of two compressible Neo-Hookean cylinders. Deformation evolution for time steps (a) $t = 0$ ms, (b) $t = 0.87$ ms, (c) $t = 1.59$ ms, (d) $t = 2.33$ ms, (e) $t = 3.09$ ms, and (f) $t = 3.97$ ms. The colours correspond to the magnitude of the Von Mises stress. Results obtained with penalty EBS with $C_c = 0.50$. It is evident from the above figures that the proposed method results in no early contact error when the two cylinders make contact.

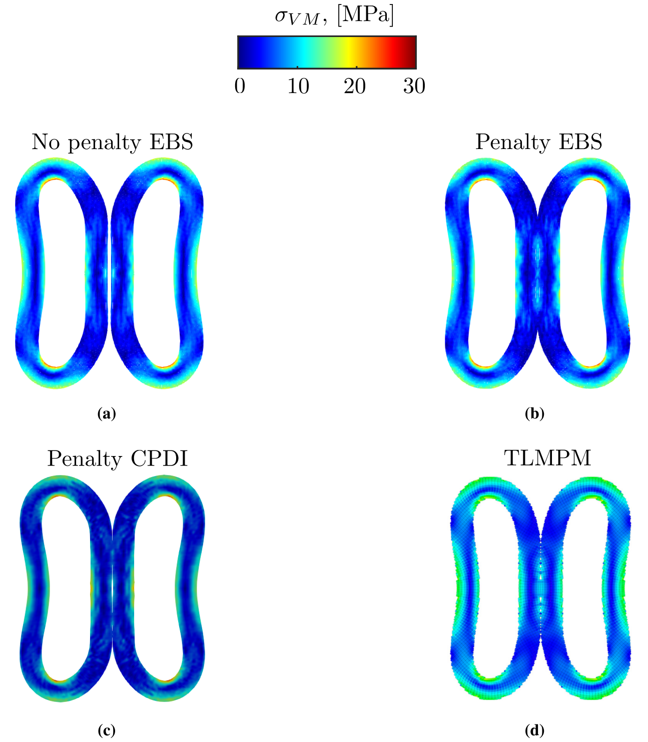

(a) (b) (c) (d)

FIGURE 26 | Impact of two compressible Neo-Hookean cylinders. Von Mises stress at time $t = 1.59$ ms for (a) no penalty EBS, (b) proposed penalty EBS, (c) penalty CPDI, and (d) TLMPM [23]. The no-penalty EBS results in early contact error, whereas the proposed penalty EBS, the penalty CPDI, and TLMPM have successfully eliminated such errors. The penalty EBS also demonstrates better energy conservation compared to TLMPM, as shown in Figure 27. The TLMPM results shown here were derived by utilising hat weighting functions, which as per [23] yield better energy conservation.

as follows

$$\mathrm{MSE} = \frac{1}{n_{steps}} \sum_{m=1}^{n_{steps}} \left(\mathcal{T}^{\mathrm{numerical}} - \mathcal{T}^{\mathrm{analytical}} \right)^2 \tag{49}$$

The MSE for the EBS method is $4 \cdot 10^{-4}$, whereas for the CPDI method it is $8 \cdot 10^{-4}$, reflecting a 50% improvement in accuracy with EBS. In comparison, the MSE for the TLMPM is 0.24. The analytical total energy is at 2 J.

4.5 | Stress Wave in a Granular Material

The previous examples focused solely on contact between two solid entities, that is, two separate discrete fields, whereas the proposed algorithm can handle multiple contacts. In this instance, we explore two significant stress wave propagation scenarios in granular media, as discussed in [17].

4.5.1 | Scenario 1

In the first scenario, four identical collinear discs are impacted by a right-travelling striker with an initial velocity of $0.0056\ \mathrm{mm}/\mu\mathrm{s}$. The geometry and boundary conditions are summarised visually in Figure 28. The problem is divided into 5 separate discrete fields, forming a total of 10 discrete pairs, as illustrated in the figure. Both the discs and the impactor are made of linear elastic material. The material properties for the impactor are $E = 17,485.71$ MPa, $\nu = 0.214$, $\rho = 1,90,000\ \mathrm{kg/m^3}$, and for each disk, they are $E = 17,4857.14$ MPa, $\nu = 0.214$, and $\rho = 1,900\ \mathrm{kg/m^3}$. Frictional contact is not employed in this configuration ($\mu_f = 0$) as there is no sliding among the discs.

The grid cell density is set at 16 material points per grid cell element for both the impactor and the discs. Three grid cell size cases are considered: (i) $\Delta h = 5$ mm, (ii) 0.025 µs, and (iii) 0.0125 µs.

Qualitative comparisons between EBS results and experimental findings from [17] are conducted. The stress distribution in the discs, assessed through photoelasticity in the experiments, is represented by dark fringes at contours of constant maximum difference in principal stresses. The simulations produce fringes using the formula:

$$\sigma_f = 1 - \sin^2\left(k_f(\sigma_1 - \sigma_2)\right) \tag{50}$$

where $k_f = \pi/0.07$ GPa. The disparity in-plane principal stress is expressed as:

$$\sigma_1 - \sigma_2 = \sqrt{4\tau_{xy}^2 + (\sigma_{xx} - \sigma_{yy})^2} \tag{51}$$

The stress fringe pattern derived through EBS is presented in Figure 29 for a time instance of 80 µs, using an occupation parameter at $C_c = 0.8$. Results from all grid spacings demonstrate a similar fringe pattern, and convergence is achieved for fine grid spacings at 2.5 and 1.25 mm. In Figure 29, the EBS-derived fringe pattern is compared against the experimental observations from [17], showing good agreement.

The energy conservation is also investigated in this multi-body contact problem. Figure 30 presents the energy results for both EBS and its CPDI counterpart for grid spacing $\Delta h = 1.25$ mm. The numerical results indicate that EBS yields in better energy in comparison to CPDI. This is more evident by evaluating the Mean Absolute Percentage Error (MAPE) as

$$\mathrm{MAPE} = \frac{1}{n_{steps}} \sum_{m=1}^{n_{steps}} \left| \frac{\mathcal{T}^{\mathrm{numerical}} - \mathcal{T}^{\mathrm{analytical}}}{\mathcal{T}^{\mathrm{analytical}}} \right| \tag{52}$$

The results, presented in Figure 31, indicate that the EBS method exhibits faster convergence rates compared to the CPDI method. Notably, the differences between the two approaches become more pronounced with coarser grid spacings. However, with mesh refinement, the accuracy of both methods becomes comparable.

4.5.2 | Scenario 2

The proposed MPM contact algorithm facilitates the inclusion of frictional contacts, thereby enabling the simulation of stress wave propagation within granular media with frictional interactions amongst constituent elements. In the second scenario, five discs

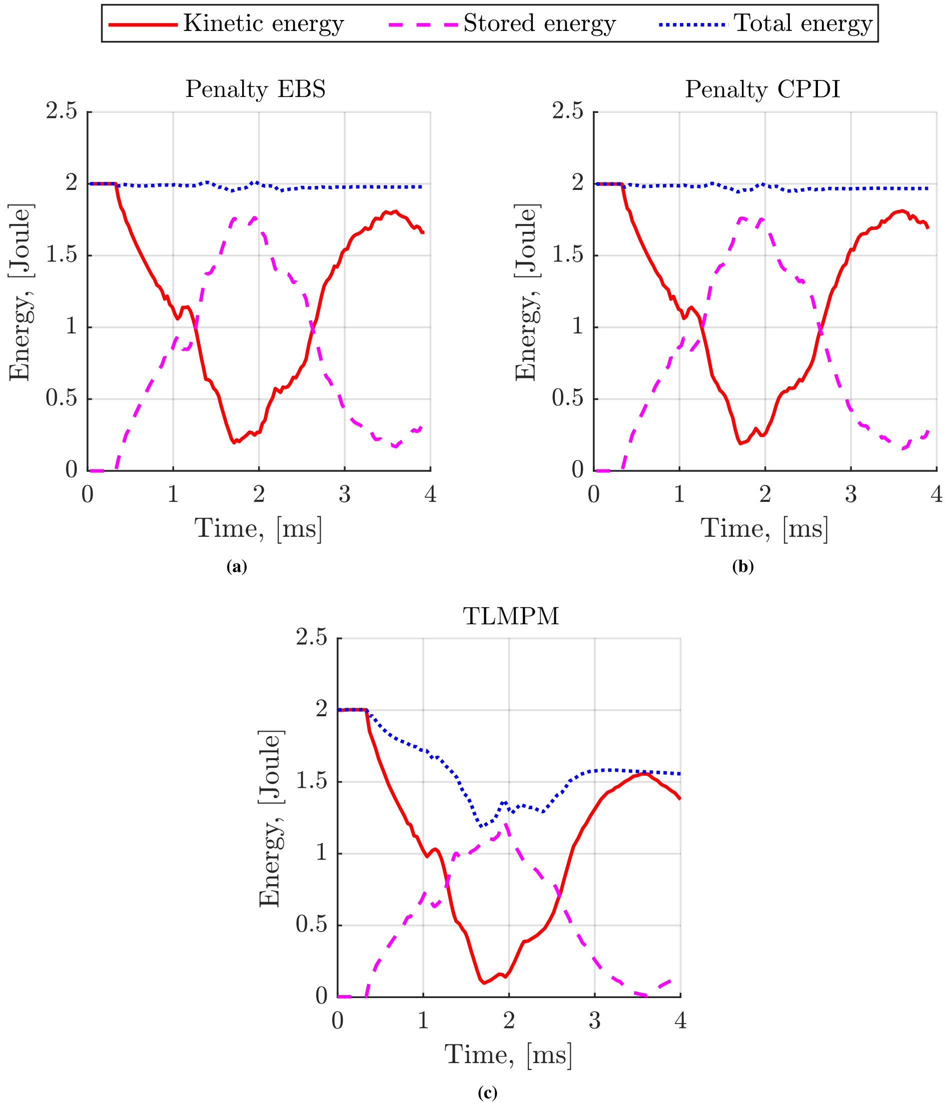

FIGURE 27 | Impact of two compressible Neo-Hookean cylinders. Kinetic, stored, and total energies for (a) penalty EBS, (b) penalty CPDI, and (c) TLMPM as proposed in [23]. The TLMPM results presented here are obtained using hat weighting functions, which, according to [23], result in enhanced energy conservation. The MSE, computed from Equation (49), for the EBS method is $4 \cdot 10^{-4}$, compared to $8 \cdot 10^{-4}$ for the CPDI method, indicating a 50% enhancement in accuracy with EBS. In contrast, the MSE for the TLMPM is 0.24. The analytical total energy is at 2 J.

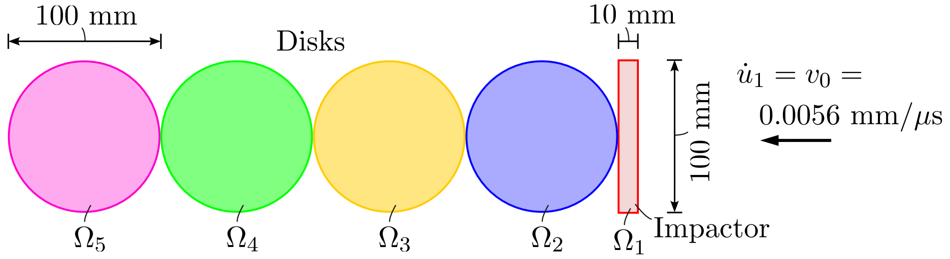

FIGURE 28 | Stress wave in granular media: Scenario 1. Geometry and boundary conditions.

mutually contacting at a 45-degree angle are subjected to impact from the right by an impactor at the established initial velocity of 0.0056 mm/μs. To prevent disc displacement, an enclosure confines them, as depicted in Figure 32. Figure 32 also shows that the problem is divided into 9 discrete fields, leading to 36 discrete pair combinations amongst them.

The disc, impactor, and their material attributes remain consistent with the four collinear disks case (Scenario 1 in Section 4.5.1). The material properties of the enclosure are chosen as in the discs for brevity. The problem's discretisation follows the previous scenario, employing three cases for the background grid cell size. Frictional contacts govern interactions between discs and between the rightmost disc and impactor, characterised by a friction coefficient $\mu_f = 0.5$. Contacts between discs and the box remain frictionless (i.e., $\mu_f = 0$).

As evident from Figure 33, a good agreement is observed between the EBS simulation results and experimental data from [17]. The EBS results are obtained for $\Delta h = 1.25$ mm and an occupation parameter at $C_c = 0.8$. Moreover, Figure 33 presents the stress fringe pattern sensitivity over grid spacing. All grid spacing cases lead to good agreement with the experimental data, and convergence is achieved for the fine grid spacing at 1.25 mm.

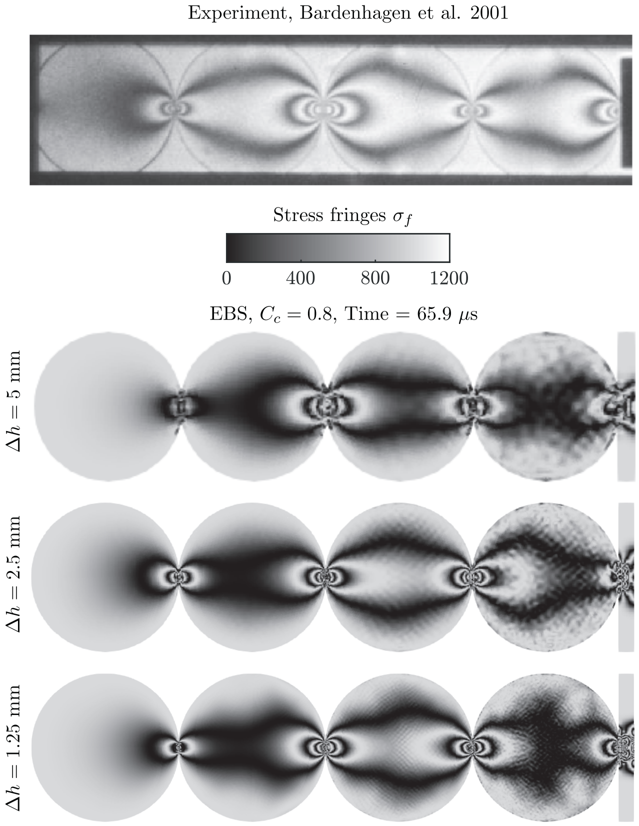

FIGURE 29 | Stress wave in granular media: Scenario 1. The stress fringe pattern derived through EBS at time instance 65.9 μs and the three grid spacing cases. The findings obtained from EBS yield good agreement with the experimental data from [17].

5 | Conclusions

This paper introduces a novel contact algorithm for the material point method. It employs a penalty-based material point-to-segment contact force calculation approach. Local calculation of the normal contact force on both surfaces is achieved

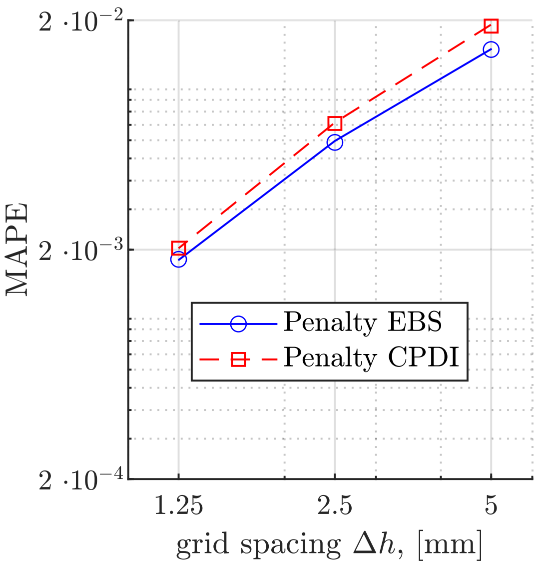

FIGURE 31 | Stress wave in granular media: Scenario 1. The results demonstrate that the EBS method achieves faster convergence rates than the CPDI method. It is noteworthy that the disparity between the two approaches is more pronounced with coarser grid spacings. However, with increased mesh refinement, both methods attain comparable levels of accuracy.

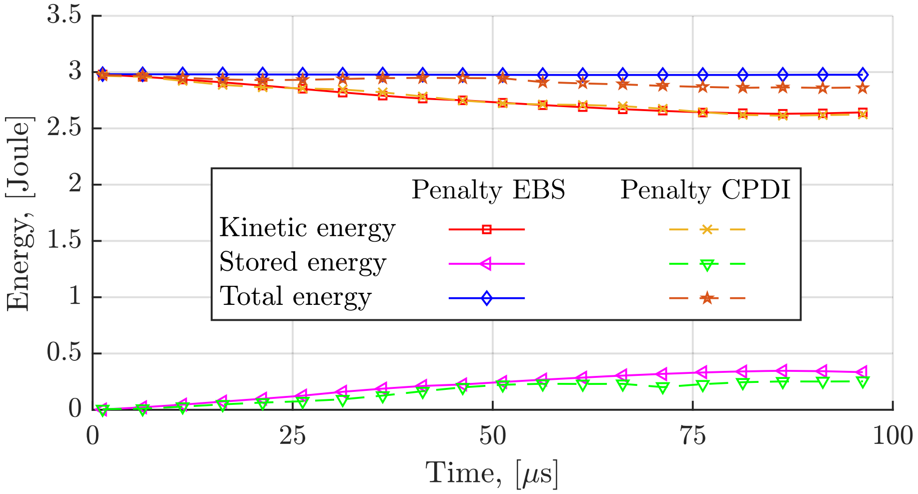

FIGURE 30 | Stress wave in granular media: Scenario 1. Energy results for both EBS and its CPDI counterpart for grid spacing $\Delta h = 1.25$ mm. The numerical results indicate that EBS yields in better energy compared to CPDI. This is also demonstrated in the MAPE plots in Figure 31.

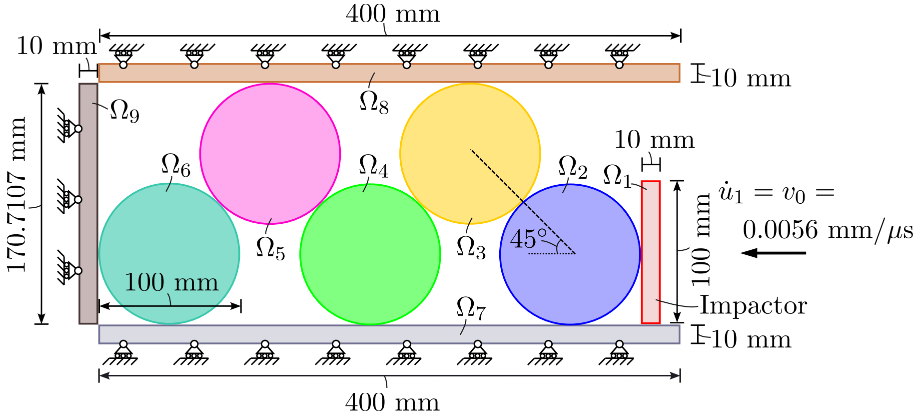

FIGURE 32 | Stress wave in granular media: Scenario 2. Geometry and boundary conditions.

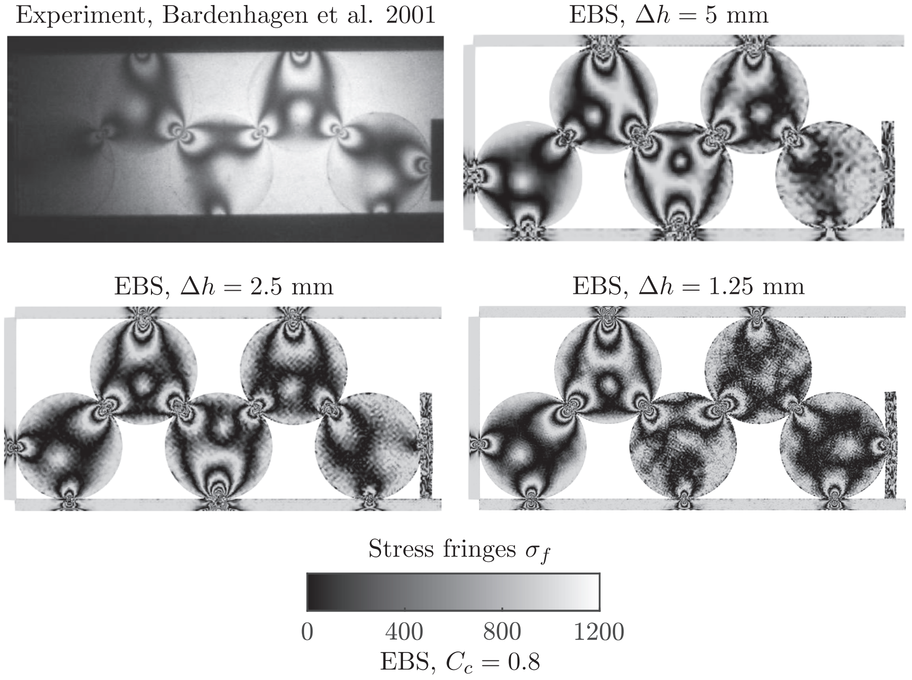

FIGURE 33 | Stress wave in granular media: Scenario 2. The stress fringe pattern derived through EBS. Results are obtained for grid spacing at 5, 2.5, and 1.25 mm. Results from all grid spacings demonstrate a similar fringe pattern, and convergence is achieved for the fine grid spacing at 1.25 mm.

using a normal gap function, while the tangential contact force is computed with a tangential slip function and the Coulomb friction model. This approach improves the representation of the contact surface, preventing premature and unrealistic body contact, a limitation observed in standard MPM contact algorithms. The proposed MPM-based contact algorithm is enhanced with EBSs, addressing significant challenges such as cell-crossing and incomplete numerical integration at certain grid cells. This enrichment improves the accuracy of contact stress estimates.

The proposed method's advantages are demonstrated through various numerical examples, leading to the following conclusions.

- The method can be easily applied to solve contact problems without significantly increasing computational complexity. Its implementation only necessitates minor modifications to the standard MPM algorithm, specifically in the areas of basis function evaluation and handling of contact features. Furthermore, boundary tracking incurs minimal computational costs, rendering it suitable for large-scale simulations, as demonstrated in this work.
- The method is verified against analytical solutions and validated against experimental observations, where it yields good agreement with them.
- It is also compared to the standard B-Spline implementation, referred to as OBS in this work, which results in a significant improvement in the stress estimates at the contact surface.
- The proposed penalty contact algorithm is implemented within a CPDI-based framework. When comparing the EBS and CPDI methods, the EBS approach was found to provide more accurate stress estimates at the contact surface.

- Comparisons with other state-of-the-art MPM contact variants from the literature show that the proposed method provides improved estimates for coarser domain boundary resolutions.
- It demonstrates better energy conservation than other state-of-the-art MPM contact variants.

Future work will expand the proposed contact algorithm in three-dimensional problems and address self-contact issues. Another future direction is the extension of the method to handle contacting multiple materials at the same point, which is not feasible with the current development. Ongoing developments include the creation of quasi-static and implicit time integration variants to improve the overall efficiency of the solution procedure.

Acknowledgements

The first author is grateful to the University of Warwick for access to its high-performance computing facility. The first author also acknowledges the support of the Engineering and Physical Sciences Research Council (EPSRC)-funded HetSys "Modelling of Heterogeneous Systems" consortium (EP/S022848/1). The third author acknowledges the support of the Marie Sklodowska-Curie Individual Fellowship grant "AI2AM: Artificial Intelligence-driven topology optimisation of Additively Manufactured Composite Components", No. 101021629.

Data Availability Statement

Data sharing not applicable to this article as no datasets were generated or analysed during the current study.

Endnotes

[1] The symbol ~ indicates trial (temporal) quantities.

References

1. P. Yang, M. Zang, H. Zeng, and X. Guo, "The Interactions Between an Off-Road Tire and Granular Terrain: GPU-Based DEM-FEM Simulation and Experimental Validation," *International Journal of Mechanical Sciences* 179 (2020): 105634, https://doi.org/10.1016/J.IJMECSCI.2020.105634.

2. W. Zhang, E. E. Seylabi, and E. Taciroglu, "An ABAQUS Toolbox for Soil-Structure Interaction Analysis," *Computers and Geotechnics* 114 (2019): 103143, https://doi.org/10.1016/J.COMPGEO.2019.103143.

3. M. N. Chatzis and A. W. Smyth, "Modeling of the 3D Rocking Problem," *International Journal of Non-Linear Mechanics* 47, no. 4 (2012): 85–98, https://doi.org/10.1016/J.IJNONLINMEC.2012.02.004.

4. M. J. Marques and P. A. Martins, "Three-Dimensional Finite Element Contact Algorithm for Metal Forming," *International Journal for Numerical Methods in Engineering* 30, no. 7 (1990): 1341–1354, https://doi.org/10.1002/NME.1620300708.

5. R. A. Sauer, "Local Finite Element Enrichment Strategies for 2D Contact Computations and a Corresponding Post-Processing Scheme," *Computational Mechanics* 52, no. 2 (2013): 301–319, https://doi.org/10.1007/S00466-012-0813-8.

6. T. X. Duong, L. De Lorenzis, and R. A. Sauer, "A Segmentation-Free Isogeometric Extended Mortar Contact Method," *Computational Mechanics* 63 (2019): 383–407, https://doi.org/10.1007/s00466-018-1599-0.

7. T. A. Laursen, M. A. Puso, and J. Sanders, "Mortar Contact Formulations for Deformable-Deformable Contact: Past Contributions and New Extensions for Enriched and Embedded Interface Formulations," *Computer Methods in Applied Mechanics and Engineering* 205-208, no. 1 (2012): 3–15, https://doi.org/10.1016/J.CMA.2010.09.006.

8. A. Scolaro, C. Fiorina, I. Clifford, and A. Pautz, "Development of a Semi-Implicit Contact Methodology for Finite Volume Stress Solvers," *International Journal for Numerical Methods in Engineering* 123, no. 2 (2022): 309–338, https://doi.org/10.1002/nme.6857.

9. W. Xing, C. Song, and F. Tin-Loi, "A Scaled Boundary Finite Element Based Node-To-Node Scheme for 2D Frictional Contact Problems," *Computer Methods in Applied Mechanics and Engineering* 333 (2018): 114–146, https://doi.org/10.1016/J.CMA.2018.01.012.

10. F. Aldakheel, B. Hudobivnik, E. Artioli, B. Veiga, and P. Wriggers, "Curvilinear Virtual Elements for Contact Mechanics," *Computer Methods in Applied Mechanics and Engineering* 372 (2020): 113394, https://doi.org/10.1016/J.CMA.2020.113394.

11. A. Popp, M. W. Gee, and W. A. Wall, "A Finite Deformation Mortar Contact Formulation Using a Primal-Dual Active Set Strategy," *International Journal for Numerical Methods in Engineering* 79, no. 11 (2009): 1354–1391, https://doi.org/10.1002/nme.2614.

12. L. De Lorenzis, P. Wriggers, and G. Zavarise, "A Mortar Formulation for 3D Large Deformation Contact Using NURBS-Based Isogeometric Analysis and the Augmented Lagrangian Method," *Computational Mechanics* 49 (2012): 1–20, https://doi.org/10.1007/s00466-011-0623-4.

13. C. PavanaChand and R. KrishnaKumar, "Remeshing Issues in the Finite Element Analysis of Metal Forming Problems," *Journal of Materials Processing Technology* 75, no. 1 (1998): 63–74, https://doi.org/10.1016/S0924-0136(97)00293-8.

14. D. Sulsky, Z. Chen, and H. L. Schreyer, "A Particle Method for History-Dependent Materials," *Computer Methods in Applied Mechanics and Engineering* 118, no. 1-2 (1994): 179–196, https://doi.org/10.1016/0045-7825(94)90112-0.

15. L. Wang, W. M. Coombs, C. E. Augarde, et al., "On the Use of Domain-Based Material Point Methods for Problems Involving Large Distortion," *Computer Methods in Applied Mechanics and Engineering* 355 (2019): 1003–1025, https://doi.org/10.1016/J.CMA.2019.07.011.

16. W. M. Coombs, C. E. Augarde, A. J. Brennan, et al., "On Lagrangian Mechanics and the Implicit Material Point Method for Large Deformation Elasto-Plasticity," *Computer Methods in Applied Mechanics and Engineering* 358 (2020): 112622, https://doi.org/10.1016/J.CMA.2019.112622.

17. S. G. Bardenhagen, J. E. Guilkey, K. M. Roessig, J. U. Brackbill, W. M. Witzel, and J. C. Foster, "An Improved Contact Algorithm for the Material Point Method and Application to Stress Propagation in Granular Material," *Computer Modeling in Engineering and Sciences* 2, no. 4 (2001): 509–522, https://doi.org/10.3970/cmes.2001.002.509.

18. M. A. Homel and E. B. Herbold, "Field-Gradient Partitioning for Fracture and Frictional Contact in the Material Point Method," *International Journal for Numerical Methods in Engineering* 109, no. 7 (2017): 1013–1044, https://doi.org/10.1002/nme.5317.

19. E. G. Kakouris and S. P. Triantafyllou, "Phase-Field Material Point Method for Dynamic Brittle Fracture With Isotropic and Anisotropic Surface Energy," *Computer Methods in Applied Mechanics and Engineering* 357 (2019): 112503, https://doi.org/10.1016/j.cma.2019.06.014.

20. G. Moutsanidis, D. Kamensky, D. Z. Zhang, Y. Bazilevs, and C. C. Long, "Modeling Strong Discontinuities in the Material Point Method Using a Single Velocity Field," *Computer Methods in Applied Mechanics and Engineering* 345 (2019): 584–601, https://doi.org/10.1016/j.cma.2018.11.005.

21. J. A. Nairn, C. C. Hammerquist, and G. D. Smith, "New Material Point Method Contact Algorithms for Improved Accuracy, Large-Deformation Problems, and Proper Null-Space Filtering," *Computer Methods in Applied Mechanics and Engineering* 362 (2020): 112859, https://doi.org/10.1016/J.CMA.2020.112859.

22. M. Xiao, C. Liu, and W. C. Sun, "DP-MPM: Domain Partitioning Material Point Method for Evolving Multi-Body Thermal-Mechanical Contacts During Dynamic Fracture and Fragmentation," *Computer Methods in Applied Mechanics and Engineering* 385 (2021): 114063, https://doi.org/10.1016/J.CMA.2021.114063.

23. d. A. Vaucorbeil and V. P. Nguyen, "Modelling Contacts With a Total Lagrangian Material Point Method," *Computer Methods in Applied Mechanics and Engineering* 373 (2021): 113503, https://doi.org/10.1016/J.CMA.2020.113503.

24. J. Guilkey, R. Lander, and L. Bonnell, "A Hybrid Penalty and Grid Based Contact Method for the Material Point Method," *Computer Methods in Applied Mechanics and Engineering* 379 (2021): 113739, https://doi.org/10.1016/J.CMA.2021.113739.

25. Y. Yamaguchi, S. Moriguchi, and K. Terada, "Extended B-Spline-Based Implicit Material Point Method," *International Journal for Numerical Methods in Engineering* 122, no. 7 (2021): 1746–1769, https://doi.org/10.1002/nme.6598.

26. F. Hamad, S. Giridharan, and C. Moormann, "A Penalty Function Method for Modelling Frictional Contact in MPM," *Procedia Engineering* 175 (2017): 116–123, https://doi.org/10.1016/J.PROENG.2017.01.038.

27. P. Huang, X. Zhang, S. Ma, and X. Huang, "Contact Algorithms for the Material Point Method in Impact and Penetration Simulation," *International Journal for Numerical Methods in Engineering* 85, no. 4 (2011): 498–517, https://doi.org/10.1002/nme.2981.

28. C. Liu and W. C. Sun, "ILS-MPM: An Implicit Level-Set-Based Material Point Method for Frictional Particulate Contact Mechanics of Deformable Particles," *Computer Methods in Applied Mechanics and Engineering* 369 (2020): 113168, https://doi.org/10.1016/J.CMA.2020.113168.

29. G. Zavarise and P. Wriggers, "A Segment-To-Segment Contact Strategy," *Mathematical and Computer Modelling* 28 (1998): 497–515, https://doi.org/10.1016/S0895-7177(98)00138-1.

30. J. Guilkey, O. Alsolaiman, R. Lander, L. Bonnell, and J. Cook, "Cohesive Zones to Model Bonding in Granular Material With the Material Point Method," *Computer Methods in Applied Mechanics and Engineering* 415 (2023): 116260, https://doi.org/10.1016/J.CMA.2023.116260.

31. H. Chen, S. Zhao, J. Zhao, and X. Zhou, "DEM-Enriched Contact Approach for Material Point Method," *Computer Methods in Applied Mechanics and Engineering* 404 (2023): 115814, https://doi.org/10.1016/J.CMA.2022.115814.

32. G. Zavarise and L. De Lorenzis, "A Modified Node-To-Segment Algorithm Passing the Contact Patch Test," *International Journal for Numerical Methods in Engineering* 79 (2009): 379–416, https://doi.org/10.1002/nme.2559.

33. S. Bardenhagen and E. Kober, "The Generalized Interpolation Material Point Method," *CMES-Computer Modeling in Engineering & Sciences* 5 (2004): 477–495, https://doi.org/10.3970/CMES.2004.005.477.

34. T. J. Charlton, W. M. Coombs, and C. E. Augarde, "iGIMP: An Implicit Generalised Interpolation Material Point Method for Large Deformations," *Computers and Structures* 190 (2017): 108–125, https://doi.org/10.1016/J.COMPSTRUC.2017.05.004.

35. A. Sadeghirad, R. M. Brannon, and J. Burghardt, "A Convected Particle Domain Interpolation Technique to Extend Applicability of the Material Point Method for Problems Involving Massive Deformations," *International Journal for Numerical Methods in Engineering* 86, no. 12 (2011): 1435–1456, https://doi.org/10.1002/NME.3110.

36. Q. A. Tran, W. Sołowski, M. Berzins, and J. Guilkey, "A Convected Particle Least Square Interpolation Material Point Method," *International Journal for Numerical Methods in Engineering* 121, no. 6 (2020): 1068–1100, https://doi.org/10.1002/NME.6257.

37. A. Sadeghirad, R. M. Brannon, and J. E. Guilkey, "Second-Order Convected Particle Domain Interpolation (CPDI2) With Enrichment for Weak Discontinuities at Material Interfaces," *International Journal for Numerical Methods in Engineering* 95, no. 11 (2013): 928–952, https://doi.org/10.1002/NME.4526.

38. P. Wilson, R. Wüchner, and D. Fernando, "Distillation of the Material Point Method Cell Crossing Error Leading to a Novel Quadrature-Based C0 Remedy," *International Journal for Numerical Methods in Engineering* 122, no. 6 (2021): 1513–1537, https://doi.org/10.1002/NME.6588.

39. Y. Liang, X. Zhang, and Y. Liu, "An Efficient Staggered Grid Material Point Method," *Computer Methods in Applied Mechanics and Engineering* 352 (2019): 85–109, https://doi.org/10.1016/J.CMA.2019.04.024.

40. Y. Bing, M. Cortis, T. J. Charlton, W. M. Coombs, and C. E. Augarde, "B-Spline Based Boundary Conditions in the Material Point Method," *Computers & Structures* 212 (2019): 257–274, https://doi.org/10.1016/J.COMPSTRUC.2018.11.003.

41. G. Moutsanidis, C. C. Long, and Y. Bazilevs, "IGA-MPM: The Isogeometric Material Point Method," *Computer Methods in Applied Mechanics and Engineering* 372 (2020): 113346, https://doi.org/10.1016/j.cma.2020.113346.

42. D. Sulsky, S. J. Zhou, and H. L. Schreyer, "Application of a Particle-In-Cell Method to Solid Mechanics," *Computer Physics Communications* 87, no. 1-2 (1995): 236–252, https://doi.org/10.1016/0010-4655(94)00170-7.

43. V. P. Nguyen, A. de Vaucorbeil, and S. Bordas, *The Material Point Method* (Springer International Publishing, 2023).

44. A. Ali Madadi and B. Dortdivanlioglu, "A Subdivision-Stabilized B-Spline Mixed Material Point Method," *Computer Methods in Applied Mechanics and Engineering* 418 (2024): 116567, https://doi.org/10.1016/j.cma.2023.116567.

45. M. Ashkan Ali and B. Dortdivanlioglu, "Mechanics of Polymeric Porous Membranes Using Stabilized Extended B-Spline Material Point," 2024. 15th Annual MPM Workshop.

46. P. Wriggers, *Computational Contact Mechanics*, vol. 2 ed. T. A. Laursen (Springer, 2006).

47. J. Bonet and R. D. Wood, *Nonlinear Continuum Mechanics for Finite Element Analysis*, 2nd ed. (Cambridge University Press, 2008).

48. L. De Lorenzis, I. Temizer, P. Wriggers, and G. Zavarise, "A Large Deformation Frictional Contact Formulation Using NURBS-Based Isogeometric Analysis," *International Journal for Numerical Methods in Engineering* 87, no. 13 (2011): 1278–1300, https://doi.org/10.1002/NME.3159.

49. T. Hughes, J. Cottrell, and Y. Bazilevs, "Isogeometric Analysis: CAD, Finite Elements, NURBS, Exact Geometry and Mesh Refinement," *Computer Methods in Applied Mechanics and Engineering* 194, no. 39-41 (2005): 4135–4195, https://doi.org/10.1016/J.CMA.2004.10.008.

50. E. G. Kakouris and S. P. Triantafyllou, "Material Point Method for Crack Propagation in Anisotropic Media: A Phase Field Approach," *Archive of Applied Mechanics* 88 (2018): 287–316, https://doi.org/10.1007/s00419-017-1272-7.

51. J. A. Nairn, S. G. Bardenhagen, G. D. Smith, and A. Nairn JohnNairn, "Generalized Contact and Improved Frictional Heating in the Material Point Method," *Computational Particle Mechanics* 5 (2018): 285–296, https://doi.org/10.1007/s40571-017-0168-1.

52. C. C. Hammerquist and J. A. Nairn, "A New Method for Material Point Method Particle Updates That Reduces Noise and Enhances Stability," *Computer Methods in Applied Mechanics and Engineering* 318 (2017): 724–738, https://doi.org/10.1016/J.CMA.2017.01.035.

53. C. Jiang, C. Schroeder, and J. Teran, "An Angular Momentum Conserving Affine-Particle-In-Cell Method," *Journal of Computational Physics* 338 (2017): 137–164, https://doi.org/10.1016/J.JCP.2017.02.050.

54. G. Pretti, W. M. Coombs, C. E. Augarde, B. Sims, M. Marchena Puigvert, and J. A. R. Gutiérrez, "A Conservation Law Consistent Updated Lagrangian Material Point Method for Dynamic Analysis," *Journal of*

Computational Physics 485 (2023): 112075, https://doi.org/10.1016/J.JCP.2023.112075.

55. N. Kikuchi and J. T. Oden, *Contact Problems in Elasticity: A Study of Variational Inequalities and Finite Element Methods* (Society for Industrial and Applied Mathematics (SIAM), 1988).

56. A. Leichner, H. Andrä, and B. Simeon, "A Contact Algorithm for Voxel-Based Meshes Using an Implicit Boundary Representation," *Computer Methods in Applied Mechanics and Engineering* 352 (2019): 276–299, https://doi.org/10.1016/J.CMA.2019.04.008.

57. D. Z. Zhang, X. Ma, and P. T. Giguere, "Material Point Method Enhanced by Modified Gradient of Shape Function," *Journal of Computational Physics* 230, no. 16 (2011): 6379–6398, https://doi.org/10.1016/J.JCP.2011.04.032.

58. K. L. Johnson, *Contact Mechanics* (Cambridge University Press, 1985).

Appendix A

Auxiliary Vectors for Contact Enforcement

In the two-dimensional case, matrices $\mathbf{C}^{nor}$ and $\mathbf{C}^{tan}$ are defined as

$$ {}^{(t)}\mathbf{C}^{nor} = -\left({}^{(t)}\mathbf{N} - \frac{{}^{(t)}g^{nor}}{{}^{(t)}l_{ms}} \, {}^{(t)}\mathbf{P} \right) \tag{A1} $$

and

$$ {}^{(t)}\mathbf{C}^{tan} = {}^{(t)}\mathbf{T} - \frac{{}^{(t)}g^{tan}}{{}^{(t)}l_{ms}} \, {}^{(t)}\mathbf{Q} \tag{A2} $$

respectively. Additionally, the **N**, **Q**, **T**, and **P** matrices assume the following form

$$ \begin{cases} {}^{(t)}\mathbf{N} = \begin{bmatrix} {}^{(t)}\mathbf{e}^{nor} \\ -(1 - {}^{(t)}\beta)\, {}^{(t)}\mathbf{e}^{nor} \\ -\, {}^{(t)}\beta \, {}^{(t)}\mathbf{e}^{nor} \end{bmatrix} & \text{(A3a)} \\ {}^{(t)}\mathbf{Q} = \begin{bmatrix} \mathbf{0} \\ -\, {}^{(t)}\mathbf{e}^{tan} \\ {}^{(t)}\mathbf{e}^{tan} \end{bmatrix} & \text{(A3b)} \\ {}^{(t)}\mathbf{T} = \begin{bmatrix} {}^{(t)}\mathbf{e}^{tan} \\ -(1 - {}^{(t)}\beta)\, {}^{(t)}\mathbf{e}^{tan} \\ -\, {}^{(t)}\beta \, {}^{(t)}\mathbf{e}^{tan} \end{bmatrix} & \text{(A3c)} \\ {}^{(t)}\mathbf{P} = \begin{bmatrix} \mathbf{0} \\ -\, {}^{(t)}\mathbf{e}^{nor} \\ {}^{(t)}\mathbf{e}^{nor} \end{bmatrix} & \text{(A3d)} \end{cases} $$

with

$$ {}^{(t)}\mathbf{u} = \begin{bmatrix} {}^{(t)}\mathbf{u}_s \\ {}^{(t)}\mathbf{u}_1 \\ {}^{(t)}\mathbf{u}_2 \end{bmatrix} \tag{A4} $$

Equations (A1)–(A4) correspond to a discretised domain boundary formed by linear segments as explained in Section 3.4. The matrices $\mathbf{C}^{nor}$ and $\mathbf{C}^{tan}$ for the one-dimensional case can be derived in a similar manner.